Non-linear electron transport studied with quantum point contacts

Brugmans, M.J.P.

Award date:
1991

Non-Linear Electron Transport studied with Quantum Point Contacts

Marco J.P. Brugmans

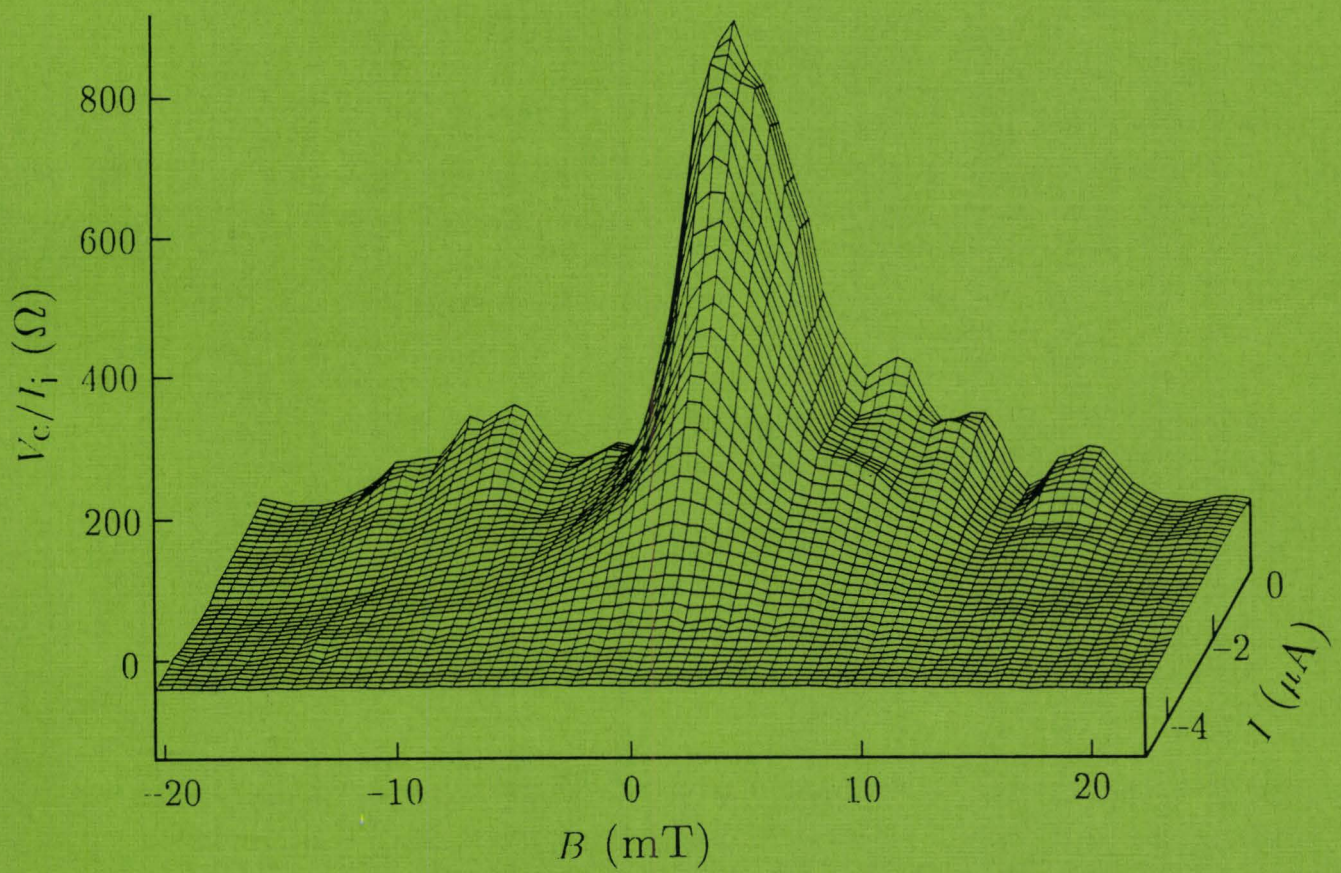

Non-Linear Electron Transport studied with Quantum Point Contacts

Marco J.P. Brugmans

Afstudeerverslag Technische Universiteit Eindhoven

Eindhoven, april 1991.

Afstudeerhoogleraar (TUE): Prof. Dr. J.H. Wolter.

Begeleider (Philips Nat. Lab.): Dr. L.W. Molenkamp.

aan Suzanne

Abstract

We present experiments on two dimensional electron transport in high mobility (Al,Ga)As-GaAs heterostructures, using quantum point contacts, electrostatically defined in the 2DEGs by means of split gates, as electron injectors and detectors.

Electrostatic manipulation of a collimated electron beam, injected by a point contact, is attempted by means of applying different voltages to the two split gates defining the point contact, to scan the point contacts in lateral direction. Although the transmission of ballistic electrons through three point contacts in series is affected by the asymmetric gate voltages, impurity effects prohibit manipulation on a highly controlled level.

Using an electrical current to selectively heat a narrow channel fitted with quantum point contacts, we observe for the first time a quantized thermal conductance of a quantum point contact. The thermal conductance increases stepwise with increasing point contact width and lines up with the quantized electrical conductance, as expected from the Wiedemann-Franz law.

The breakdown of the quantum Hall effect in a narrow channel at high current densities can be controlled by adjusting the transmission probabilities of point contacts at the high electrochemical potential edge of the channel. We find that breakdown occurs predominantly by backscattering within the uppermost Landau level.

Electron beam collimation is used as a probe for electron–electron interactions as function of electron temperature in the ballistic regime. In this new regime the electron–electron mean free path is shorter than the transport mean free path, and agrees reasonably with the scattering length calculated from Fermi liquid theory.

Contents

Chapter 1

Introduction

The two dimensional electron gas (2DEG), a sheet of conducting electrons at the interface of a semiconductor heterostructure, has been studied extensively as a model system for low dimensional electron transport at low temperatures. These heterostructures, modulation doped (Al,Ga)As–GaAs in our case, are grown with molecular beam epitaxy (MBE) or organo-metallic vapour phase epitaxy (OMVPE). The crystal growth in these fabrication techniques is controlled at the atomic level yielding materials of extreme purity. The improvement of these techniques, a consequence of the industrial strive for smaller and faster electronic devices, has resulted in a decrease in impurity scattering and hence an increase of the mobility μ of these 2DEGs. Typically, the mobility for (Al,Ga)As–GaAs grown by MBE at the Philips Research Laboratories, Redhill England, nowadays is $\mu > 1 \times 10^6$ cm^2/Vs. With a typical sheet carrier concentration of $n_s = 3 \times 10^{11}$ cm^{-1} this yields an electron mean free path $l_e > 9\mu$m.

It is only very recent that the development of this high quality material and the availability of sophisticated lithographic techniques to produce structures in the 2DEG on sub-micron scale, allow the study of electron transport in the *ballistic* regime, where the transport properties are completely determined by the geometry of the constriction, see Figure 1.1. This in contrast to the conventional diffusive electron transport, where impurity collisions govern the transport properties. The ballistic regime was entered in 1988 by the fabrication of a *quantum point contact* in a 2DEG by Van Wees *et al.* [1] and by Wharam *et al.* [2]. The point contact, a constriction in the 2DEG with length L and width W smaller than the mean free path l_e, not only shows ballistic transport but it also exhibits *quantum size effects.* The conductance of a quantum point contact in absence of a magnetic field is quantized in integer steps of $2e^2/h$. This quantum effect arises because the width of the quantum point contact is of the order of the electron Fermi wavelength $\lambda_F = 2\pi/k_F$ with the Fermi wave vector (for (Al,Ga)As–GaAs) given by $k_F = (2\pi n_s)^{1/2}$. This implies quantization of the electron momentum normal to the constriction resulting in quasi one-dimensional electron transport across a quantum

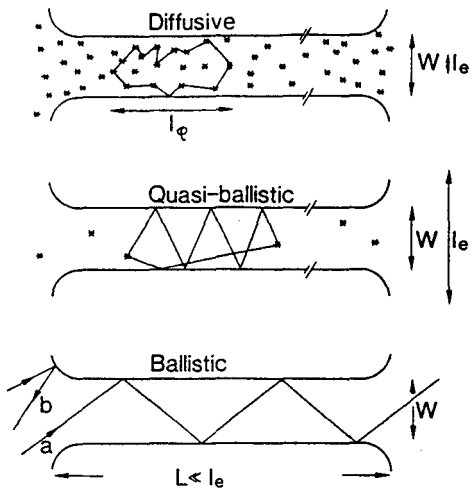

Figure 1.1: Electron trajectories characteristic for the diffusive ($l_e < W, L$), quasi-ballistic ($W < l_e < L$) and ballistic ($W, L < l_e$) transport regimes, for the case of specular boundary scattering. Impurity scattering is denoted with asterisks. A non-zero resistance in the ballistic regime results from backscattering at the connection between the narrow channel and the wide 2DEG regions.

point contact. Note that this quantum regime can not yet be achieved in metals, for which $\lambda_F \sim 0.1$ nm.

Since the discovery of quantum point contacts in a 2DEG much work has been done in quantum ballistic transport and in adiabatic transport, where due to the magnetic field transport takes place along quasi one-dimensional edge channels, see Refs. [3,4]. In these studies, the point contacts are used as adjustable current sources and/or voltage probes, yielding new and detailed information on the transport processes. Hot topics in this field are nowadays electron–electron interactions (*e.g.* Coulomb blockade), and non-linear effects in the quantum ballistic and adiabatic regimes. Recently, *e.g.*, quantum oscillations in the non-linear regime were observed experimentally and interpreted as oscillations in the thermovoltage of a quantum point contact [5].

In this report we present some studies in the non-linear regime, using quantum point contacts, electrostatically defined in a 2DEG by means of the split gate technique, as voltage probes and electron injectors. Chapter 2 is a comprehensive review of those aspects of quantum point contacts that will be used later on. The experimental set-up is presented in Chapter 3. Although the main subject of this report is non-linear electron transport, we have also attempted to manipulate collimated electron beams in the 2DEG electrostatically. For the sake of completeness this study, which concerns transport in the *linear* response regime, is described in Chapter 4. Chapter 5 discusses the observation of the quantized thermal conductance of a quantum point contact. Breakdown of the

quantum Hall effect in a narrow channel with quantum point contacts as adjustable voltage probes at the channel boundaries is presented in Chapter 6. In Chapter 7 we study a new transport regime, where electron–electron interactions determine the transport properties and where the 2D electron gas must be treated as a Fermi liquid.

Chapter 2

Quantum Point Contacts

In this chapter only a comprehensive review is given of the features of quantum point contacts that are necessary to understand the experimental studies that will be presented in following chapters. For an extensive review I refer to Refs. [3,4].

2.1 Introduction

A point contact is a small conducting orifice between two conducting reservoirs, with dimensions small compared to the mean free path. A point contact in the 2DEG of an (Al,Ga)As–GaAs heterostructure is usually created by means of split gates. On top of the heterostructure a pattern of gold gates is defined using electron-beam lithography (Fig. 2.1). By applying a negative voltage to the gates that exceeds a threshold voltage (typically -0.5 V in our samples) the 2DEG regions under the gates are depleted and the point contact is defined electrostatically. Increasing the negative voltage gradually reduces the width of the point contact and raises the bottom of the point contact region with respect to the Fermi energy, until the point contact is *pinched off*.

The 2DEG in the MBE grown $Al_xGa_{1-x}As$–GaAs ($x \approx 0.3$) heterostructure is an ideal model system because of the simple Fermi surface, which is a circle, the long mean free path at low temperatures, $l_e \approx 10$ μm, and the large Fermi wavelength, $\lambda_F \approx 40$ nm. In this report we assume that only the lowest electric 2D subband is occupied in the 2DEG due to low temperature and small electron density.

2.2 Conductance Quantization

Van Wees *et al.*[1] and Wharam *et al.*[2] independently discovered a steplike increase of the conductance G upon increasing the point contact width W, in absence of a magnetic field, see also Fig. 2.3. The observed conductance is quantized in integer steps of $2e^2/h$.

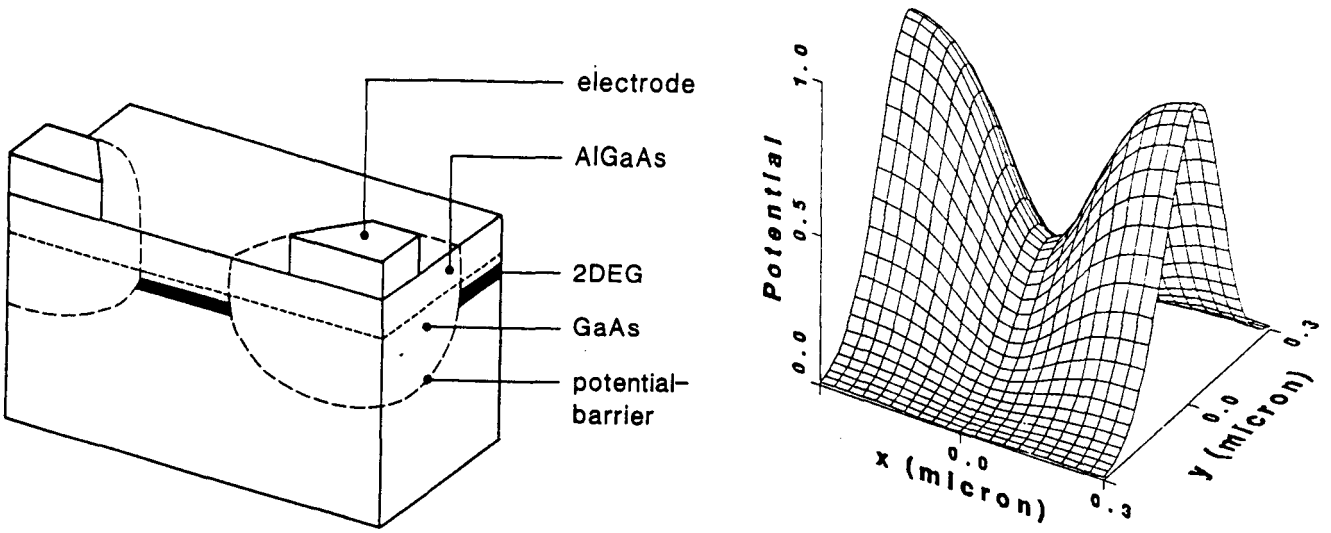

Figure 2.1: A heterostructure with on top of it the split gate structure (left). The 2DEG under the gates is depleted by a negative bias on the gates, leaving a saddle-shaped constriction, the point contact, for the conduction electrons (right). Increasing the negative bias on the gates both decreases the width and raises the bottom of the constriction potential.

Consider a *classical* ballistic point contact, connecting two reservoirs with electron densities of $n+\delta n$ and n respectively, see Fig. 2.2. At low temperatures the excess charge moves with the Fermi velocity $v_{\rm F}$. In the ballistic limit all the electrons impinging on the point contact with width W are transmitted. The total current I through the point contact follows from the incoming electron flux

$$I = \frac{1}{2} e\, \delta n\, \langle v_{\rm F} \rangle W = \frac{1}{2} e\, \delta n \left(\frac{1}{\pi} \int_{-\pi/2}^{\pi/2} v_{\rm F} \cos\phi \, {\rm d}\phi \right) W = \frac{e}{\pi} W v_{\rm F}\, \delta n \qquad (2.1)$$

where the $\langle \ldots \rangle$ denotes an angular average over the half space and ϕ is the angle with the point contact normal (Fig. 2.2). The net concentration difference δn corresponds to a chemical potential difference $\delta\mu = eV$. With the identification of $\delta n/\delta\mu$ as the density of states at the Fermi-level, for a 2DEG with spin degeneracy given by $\delta n/\delta\mu = m/\pi\hbar^2$, one finds from Eq.(2.1) for the conductance $G \equiv I/V$

$$G = \frac{2e^2}{h} \frac{k_{\rm F} W}{\pi}, \text{ in 2D} \qquad (2.2)$$

where $k_{\rm F} = m v_{\rm F}/\hbar$ is the Fermi wave vector. We will refer to Eq.(2.2) as the Sharvin conductance. This classical result, however, predicts a monotonically increasing G with W.

The observed quantized conductance is interpreted in terms of quantization of $k_{\rm F}W/\pi$ in Eq.(2.2), for $W \sim \lambda_{\rm F}$. The current injected in the conductor (point contact), due to the chemical potential difference $\delta\mu$ between the reservoirs, can only propagate through N one-dimensional subbands, or transverse modes, in the constriction. The injected current carrying states, with energies within $\delta\mu$ above $E_{\rm F}$, now propagate through the

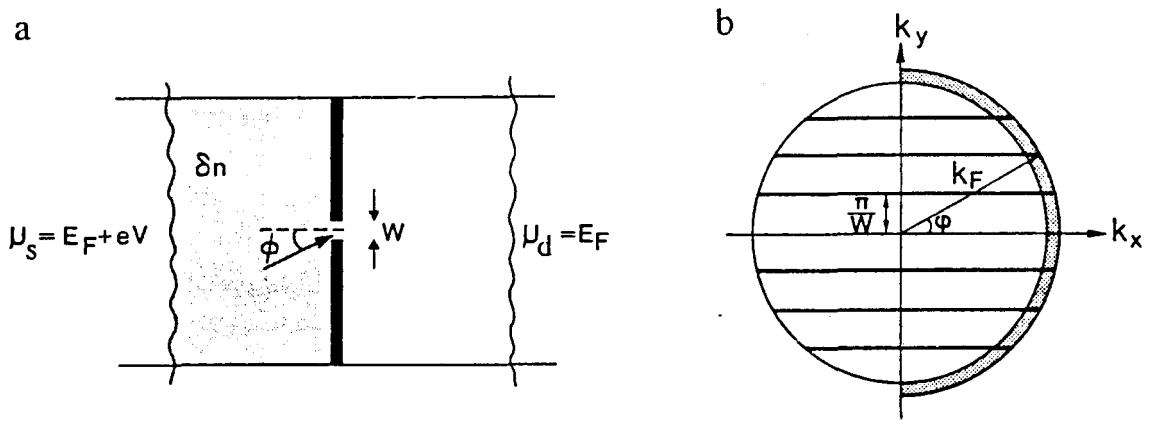

Figure 2.2: (a) Classical ballistic transport through a point contact induced by a concentration difference δn, or chemical potential difference $\delta\mu = eV$, between source (s) and drain (d). (b) The net current through a quantum point contact is carried by the shaded region in k-space. In a narrow channel the allowed states lie on horizontal lines, which correspond to quantized values for $k_y = \pm n\pi/W$, and continuous values for k_x. The formation of these 1D subbands gives rise to a quantized conductance.

constriction as indicated in Fig. 2.2 for a square well lateral confining potential of width W. In that case the one-dimensional subbands correspond in k-space to pairs of horizontal lines at $k_y = \pm n\pi/W$, with $n = 1, 2, \ldots, N$ and $N = \mathrm{Int}(k_F W/\pi)$. The current per unit energy interval injected into a subband is the product of the group velocity and the one-dimensional density of states. The group velocity is $v_n = \mathrm{d}E_n(k)/\hbar \mathrm{d}k$ and the density of states for one velocity direction and including spin degeneracy is $\rho_n = (\pi \mathrm{d}E_n(k)/\mathrm{d}k)^{-1}$. The product of v_n and ρ_n is seen to be independent of both energy and subband index n. Thus the injected current is distributed among the subbands, each subband carrying the same amount of current $ev_n\rho_n\delta\mu = (2e/h)\delta\mu$. Note that this equipartitioning of current holds irrespective of the exact dispersion relation $E_n(k)$. The total current $I = (2e/h)N\delta\mu$ yields a conductance $G = eI/\delta\mu$ given by

$$G = \frac{2e^2}{h}N \tag{2.3}$$

with N the number of occupied subbands in the quantum point contact. Reducing the width of the point contact reduces N by one at the time, giving rise to the quantized conductance.

As shown in Fig. 2.3 the conductance quantization is conserved in the presence of a perpendicular magnetic field. There is a smooth transition from the zero-field conductance to the quantum Hall effect, with a gradual reduction of the number of plateaus in a gate voltage interval. Equation (2.3) holds for a non-zero magnetic field, the conductance is quantized regardless of the origin of the subbands in the constriction.

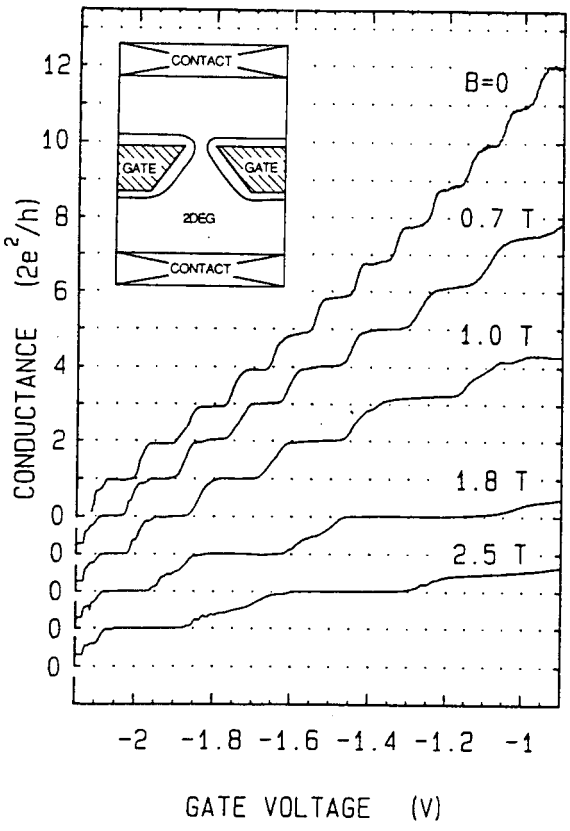

Figure 2.3: Point contact conductance (corrected for background resistance) as a function of gate voltage for several magnetic field values. The curves have been offset for clarity. The inset shows the device geometry.

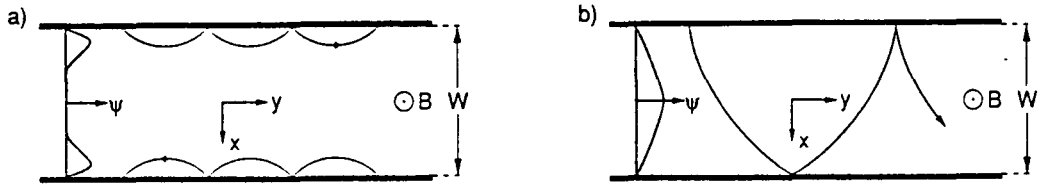

Figure 2.4: Electron trajectories in a narrow channel in a perpendicular magnetic field (right) and the corresponding transverse profile of the wave function Ψ (left). Skipping orbits on both opposite edges and the corresponding edge states are shown in (a), where $B > B_{\text{crit}}$. In (b) is $B < B_{\text{crit}}$ and is the traversing trajectory and corresponding bulk state shown.

With increasing B the electric 1D subbands turn into 1D subbands of magnetic origin in the quantum Hall regime, as is illustrated by the following.

Applying a perpendicular magnetic field to a 2DEG region forces the electrons to move in cyclotron orbits with radius $l_c = \hbar k_F/eB$ and cyclotron frequency $\omega_c = eB/m$. Beyond a critical magnetic field ($B_{\text{crit}} = 2\hbar k_F/eW$ denotes the magnetic field where the cyclotron orbit diameter equals the width W of the 2DEG region) a discrete set of energy states is formed, $E_n = (n - \frac{1}{2})\hbar\omega_c$, where n numbers the Landau levels. In the bulk 2DEG the Landau levels are zero-dimensional localized states which are classically represented by cyclotron orbits. At the 2DEG boundaries the Landau levels are manifest in 1D extended edge states, classically represented as skipping orbits, see Fig. 2.4.

The origin of the magnetic depopulation of subbands manifest in the reducing number of plateaus for a given gate voltage interval with increasing B in Fig. 2.3 is evident when the shape of Landau levels near the constriction boundaries is considered. The Landau levels follow the constriction boundaries and edge channels are formed where they cross the Fermi-energy, see Fig. 2.5. The number of occupied edge channels thus equals the number of populated bulk Landau levels, $N \approx \hbar\omega_c$, and decreases with increasing B. If the Fermi-level lies in between two Landau levels in the bulk, only the populated edge channels contribute to the current.

Regardless of the character of the 1D subbands in a point contact the conductance can be interpreted as the transmission of modes across the point contact. Let us assume that transport across the constriction is *adiabatic*, *i.e.* that there is no inter-subband scattering. This assumption is valid in the quantum Hall regime, where absence of inter-edge channel scattering is observed on macroscopic length scales, and in the zero-field case if the constriction (point contact) changes gradually in width (*i.e.* has a flaring boundary). Equation (2.3) can then be interpreted as a direct manifestation of the

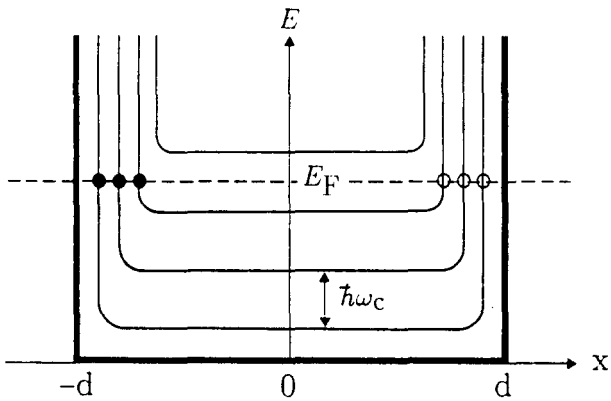

Figure 2.5: Schematic representation of Landau levels across a constriction. The Landau levels follow the boundaries where they cross the Fermi-energy, thereby creating current carrying edge channels. The edge channels at opposite boundaries, indicated by open *vs.* filled circles, have opposite directions.

two-terminal Landauer formula for quantum transport

$$G = \frac{2e^2}{h} \sum_{n=1}^{N} T_n \tag{2.4}$$

where T_n denotes the transmission probability at the Fermi energy of mode n going from one reservoir to the other. This concept has been extended by Büttiker to the multi-terminal case [6], see Fig. 2.6. Let $T_{\alpha\to\beta}$ be the total transmission probability from reservoir α to reservoir β. The number of propagating modes in the constriction connecting reservoir α is N_α. A (charge) current $(2e/h)N_\alpha\mu_\alpha$ is injected into the lead by reservoir α, which has chemical potential μ_α. A fraction $T_{\alpha\to\beta}/N_\alpha$ of that current is transmitted to reservoir β, and a fraction $T_{\alpha\to\alpha}/N_\alpha \equiv R_\alpha/N_\alpha$ is reflected back into reservoir α. The net current in lead α is thus given by

$$\frac{h}{2e} I_\alpha = (N_\alpha - R_\alpha)\mu_\alpha - \sum_{\beta(\beta\neq\alpha)} T_{\beta\to\alpha}\mu_\alpha \tag{2.5}$$

This Landauer-Büttiker formalism is a powerful tool to describe transport in the adiabatic regime. Setting the chemical potential of one reservoirs (the drain) to zero and writing down Eq.(2.5) for the currents in all the leads (or constrictions) connecting the reservoirs provides a set of equations from which the chemical potentials of all remaining reservoirs can be calculated. In this way the multi-terminal conductance (or resistance) can be obtained.

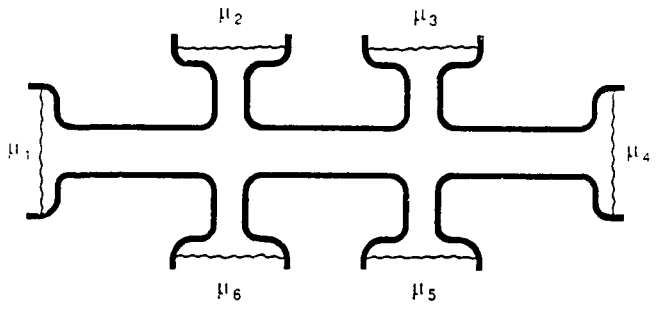

Figure 2.6: Multi-terminal geometry with six reservoirs.

2.3 Electron Beam Collimation

An unambiguous demonstration of ballistic electron transport in semiconductor nanostructures is the direct observation of a collimated electron beam by Molenkamp *et al.*[7]. Electrons are injected in a wide 2DEG region by a point contact in a beam with narrow angular distribution. In the collimation experiment [7] the injected beam is detected by sweeping the beam past a detecting point contact (the collector) by means of a magnetic field. The distance between injector and collector must be smaller than the electron mean free path (in Ref.[7] the distance was 4 μm and $l_e \approx 10$ μm). The result of this collimation experiment [7] is shown in Fig. 2.7.

Two mechanisms contribute to the electron beam collimation, as illustrated in Fig. 2.8. From the ballistic electrons, which all move with momentum $\hbar k_F$, only those electrons with enough momentum transverse to the *barrier* in the point contact can overcome that barrier and travel through the point contact. Secondly, gradual widening of the point contact at entrance and exit acts like a horn for the ballistic moving electrons through the point contact. The flaring point contact potential yields *horn collimation.* To account for these two mechanisms, let us describe the point contact potential with a minimal and maximal width, $W_{\min}$ and $W_{\max}$, and a maximum barrier height E_c above the bottom of the conduction band in the wide 2DEG regions (occurring at $W = W_{\min}$). Then a collimation factor f ($f > 1$ for collimation) can be introduced that accounts for both horn collimation and barrier collimation and which is related to the full opening angle $\Delta\alpha$ of the collimation beam

$$f = \frac{k_F}{k_{pc}} \frac{W_{\max}}{W_{\min}} \quad ; \quad \Delta\alpha = 2 \arcsin \frac{1}{f} \tag{2.6}$$

where $k_{pc} \equiv [2m(E_F - E_0)/\hbar^2]^{1/2}$ is the Fermi wave vector in the point contact.

Via the transmission probability $T_{i \to c}$ for direct travelling from the injector to collector, obtained from a semi-classical analysis, the zero-field amplitude of the collimation

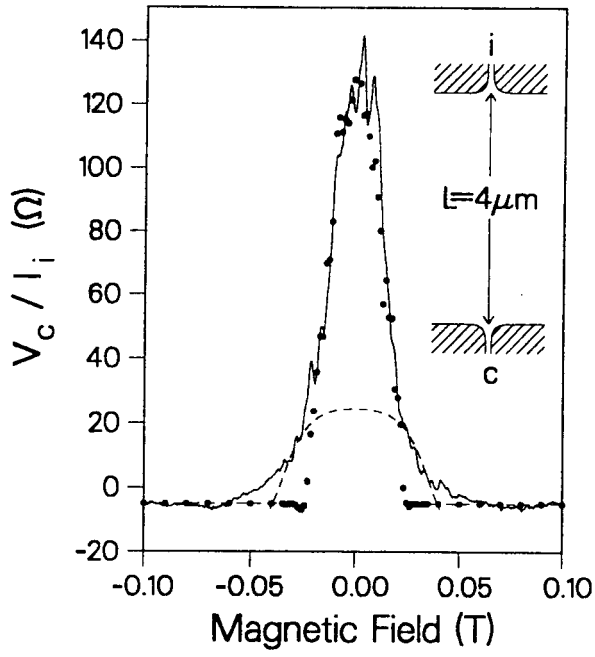

Figure 2.7: Detection of a collimated electron beam over a distance of 4 μm, using a magnetic field to sweep the injected beam past the collecting point contact. Two Ohmic contacts to the 2DEG region in between the point contacts at either side of the line connecting the injector and collector is used: One acts as a drain for the current I_i through the injector, and the other is used as a zero-reference for the voltage V_c of the collector. The solid curve is the experiment, at $T = 1.8$ K. The black dots are the result of a semi-classical simulation, using a hard-wall potential with contours as shown in the inset. The dashed curve results from a simulation without collimation (corresponding to rectangular corners in the potential contour).

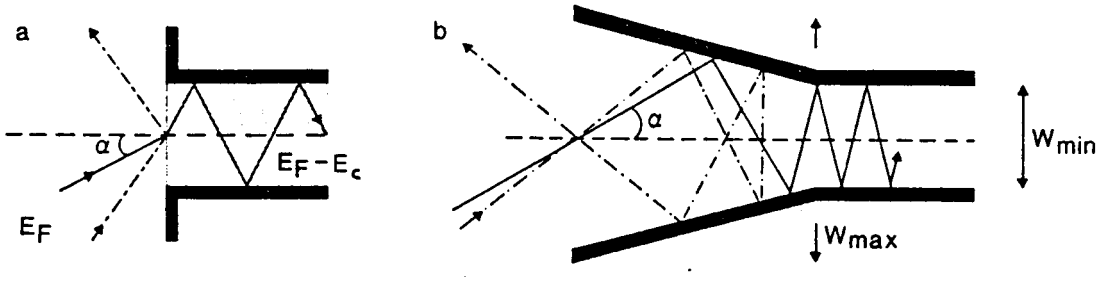

Figure 2.8: Illustration of the separate collimation effects of (a) an potential barrier of height E_c and (b) a horn-shaped constriction, which is flared from W_{min} to W_{max}. The dash-dotted trajectories approaching at an angle α outside the injection/acceptance cone are reflected.

signal of the experiment of Ref. [7] is found

$$\frac{V_c}{I_i}(B=0) = \frac{h}{2e^2}\left(f^2 - \frac{1}{2}\right)\frac{\pi}{2k_F L} \tag{2.7}$$

where L is the distance between the identical injecting and detecting point contacts. Formula (2.7) applies if one side of the intermediate 2DEG is grounded and the collector voltage is measured relative to the other side. When both sides are grounded ($f^2 - 1/2$) has to be replaced by f^2 [3,4].

The angular distribution (normalized to unity) $P(\alpha)$ of the injected electron beam, with α the angle with the axis connecting both point contacts, is in good approximation [7]

$$\begin{aligned} P(\alpha) &= \frac{1}{2} f \cos\alpha \ , \text{ if } |\alpha| < \frac{\Delta\alpha}{2} \\ P(\alpha) &= 0 \ , \text{ otherwise} \end{aligned} \tag{2.8}$$

The magnetic field at which an injected beam with angular distribution given by Eq.(2.8) is just swept past the collector is then given by

$$B_{max} = \frac{2\hbar k_F}{eL} \arcsin\frac{1}{f} \tag{2.9}$$

The collimation factor can be directly related to the point contact resistance using Eq.(2.6). From Eq.(2.3) follows $R_{pc} = h/2e^2N$ and in the semi-classical analysis used to derive $T_{i\to c}$ we have $N = k_{pc}W_{min}/\pi$, so that

$$f = R_{pc}\frac{2e^2}{h}\frac{k_F W_{max}}{\pi} \tag{2.10}$$

However, in the quantum limit, where $W_{min} \sim \lambda_F$, the semi-classical analysis is inappropriate. This limits the use of Eq.(2.10) to rather low, not quantized, point contact resistances. The experiment of Ref.[7] was performed for these low point contact resistances. In that case the barriers in the point contacts are negligible, thus the experimental trace in Fig. 2.7 is interpreted as horn collimation of a point contact.

2.4 Thermopower

According to linear transport theory in bulk solids, the electric current $\mathbf{I}$ and the thermal current $\mathbf{U}$ are linear functions of the gradients of electric field and temperature

$$\begin{aligned} \mathbf{I} &= L_{EE}\mathbf{E} + L_{ET}\nabla T \\ \mathbf{U} &= L_{TE}\mathbf{E} + L_{TT}\nabla T \end{aligned} \tag{2.11}$$

The coefficients L_{ii} are related to macroscopic transport coefficients that are measured in experiments. From $\mathbf{I} = \sigma\mathbf{E}$ with $\nabla T = 0$ follows directly for the electric conductivity

$$\sigma = L_{EE} \tag{2.12}$$

The thermal conductivity κ is determined by measuring the heat flux resulting from a temperature gradient while there is no electric current. With $\mathbf{U} = \kappa\nabla T$ and $\mathbf{I} = 0$ the thermal conductivity can be written in terms of the coefficients of Eq.(2.11)

$$\kappa = -\left(L_{TT} - \frac{L_{TE}L_{ET}}{L_{EE}}\right) \tag{2.13}$$

When $\mathbf{I} = 0$ a temperature gradient causes an electric field and hence a thermovoltage can be measured. The corresponding thermopower can be written as (using $\mathbf{E} = S\nabla T$)

$$S = -\frac{L_{ET}}{L_{EE}} \tag{2.14}$$

Finally, under the condition $\nabla T = 0$, an electric field is accompanied by an thermal current. The associated Peltier coefficient Π, $\mathbf{U} = \Pi\mathbf{I}$, is given by

$$\Pi = \frac{L_{TE}}{L_{EE}} \tag{2.15}$$

(The thermopower and Peltier coefficient are related by the Kelvin-Onsager relation $L_{ET} = -L_{TE}/T$ giving $S = \Pi/T$.)

The Eqs.(2.12)-(2.15) are derived for an homogeneous conductor for which the local and global transport coefficients are essentially the same. Although semiconductor nanostructures are not homogeneous, Butcher [8] has shown that for these systems Eqs.(2.12)-(2.15) still hold, provided that the coefficients given by Eqs.(2.12)-(2.15) are regarded as global entities. So σ is identified with the electrical conductance G, and κ is identified with the thermal conductance.

As we have seen in Section 2.2 the electrical conductance of a quantum point contact is quantized. Similar quantum effects may be expected for the other macroscopic transport coefficients discussed above, although they are not as easy to measure as σ. Streda indeed predicted a quantized thermopower in the ballistic regime [9]. The static thermopower is given by

$$S = -\frac{\Delta\mu}{e\Delta T} = \frac{k_B}{e}\frac{\int_{-\infty}^{+\infty}\frac{dn_F(E)}{dE}t(E)\frac{E-\mu}{k_BT}dE}{\int_{-\infty}^{+\infty}\frac{dn_F(E)}{dE}t(E)dE} \tag{2.16}$$

where $n_F(E)$ stands for the Fermi-Dirac distribution function, and μ and T denote the average chemical potential and temperature, respectively. The energy-dependent transmission coefficient $t(E)$ may be approximated by a step function of energy in the

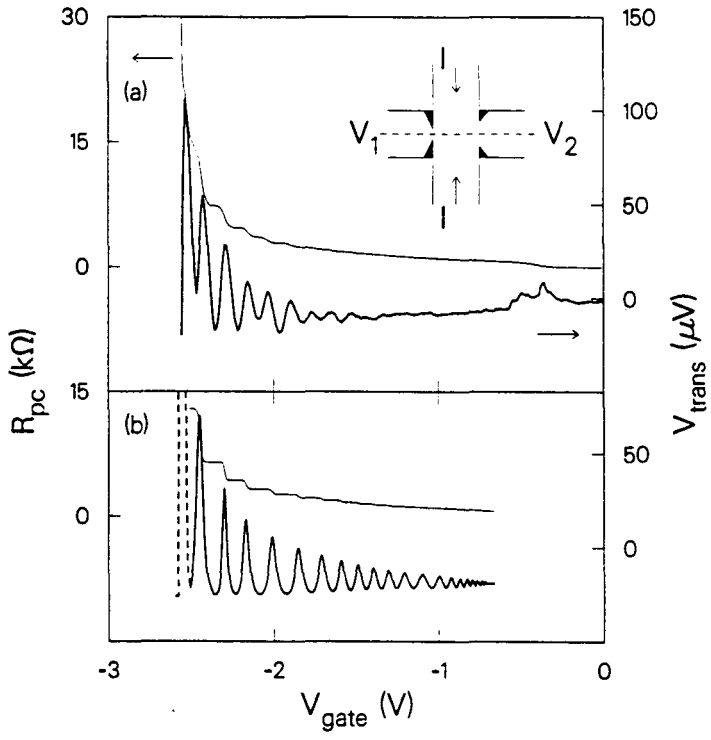

Figure 2.9: (a) Experimental trace of $V_{\rm trans}$ (thick curve) and $R_{\rm pc}$ as a function of $V_{\rm gate}$ at lattice temperature $T_0 = 1.65$ K for $I = 5$ μm and $V_{\rm gate}^{\rm ref} = -2.0$ V. Inset: arrangement for transverse voltage measurements in a channel. The point contact voltage probes are indicated in black. (b) Calculation of $V_{\rm trans}$ and $R_{\rm pc}$ as function of $V_{\rm gate}$ derived as described in the text.

quantum ballistic regime. Substituting such a $t(E)$ in Eq.(2.16) results in an oscillating thermopower of a point contact, the thermopower being zero where the conductance is at a quantized plateau and showing peaks where the number of subbands in the point contact changes by one [9].

Recently, this oscillating thermopower of a point contact has been observed experimentally by Molenkamp *et al.* [5]. In this experiment a current is passed through a 18 μm long and 4 μm wide channel. A transverse voltage is measured across two quantum point contacts in the channel boundaries. One of the point contacts merely serves as a reference voltage probe and has a fixed width during the measurement. The transverse voltage is seen to oscillate as function of the gate voltage of the opposite point contact, see Fig. 2.9. Such a transverse voltage in absence of a magnetic field is not allowed in the linear regime. The oscillations line up with the steps in the quantized resistance of the scanned point contact.

The results are interpreted as follows [5]. The current through the channel selectively heats the electron gas in the channel (Joule heating), leaving the 2DEG regions

behind the point contacts essentially in thermal equilibrium with the lattice. The lattice temperature remains uniform and is negligibly affected by the heated 2DEG region, because of the weak electron–phonon coupling at low temperatures. The energy-dependent transmission probability of the quantum point contact, $t(E)$, is larger for the hot electrons than for the cold electrons. However, since the point contact is used as a voltage probe, no net current can flow from the hot region to the cold region. This means that the cold region is charged relative to the hot region, as can be seen by rewriting the condition $I_{\mathrm{hot}\rightarrow\mathrm{cold}} = I_{\mathrm{cold}\rightarrow\mathrm{hot}}$ as

$$\frac{2e}{h}\int_0^\infty t(E)[f_{\mathrm{l}}(E) - f_{\mathrm{r}}(E)]\mathrm{d}E = 0 \tag{2.17}$$

where $f_{\mathrm{l}}(E)$ is the distribution function of electrons in the cold 2DEG region behind the point contact and $f_{\mathrm{r}}(E)$ is the electron distribution in the hot channel region, see Fig. 2.10. The distribution functions are modeled as Fermi-Dirac functions, where f_{r} has the hot electron temperature T and chemical potential E_{F}, and f_{l} has the cold lattice temperature T_0 and chemical potential $E_{\mathrm{F}} + \Delta\mu$. With these distribution functions and an appropriate choice for $t(E)$ of a quantum point contact, $\Delta\mu$ can be determined for both the scanning and the reference point contact. The transverse voltage $V_{\mathrm{trans}} = (\Delta\mu - \Delta\mu^{\mathrm{ref}})/e$ obtained from such a calculation is shown in Fig. 2.9(b), for $T = 4$ K, $T_0 = 1.65$ K and $E_{\mathrm{F}} = 13$ meV. This calculation gives a similar result as the experiment, peaks in V_{trans} are observed in both cases when the number of accessible subbands changes by one.

The amplitude and width of the peaks in the transverse voltage are sensitive to the precise shape of $t(E)$. If the quantum point is modeled as a square-well lateral-confinement potential, which is done in the calculation leading to the result shown in Fig. 2.9(b), the amplitude is given by

$$\Delta V_{\mathrm{trans}} \approx \frac{\ln(2)k_{\mathrm{B}}(T - T_0)}{eN} \tag{2.18}$$

when the transmission of the quantum point contact is $(N + \frac{1}{2})$ [5,9]. Here is assumed that $k_{\mathrm{B}}T$ is much smaller than the 1D subband spacing (~ 0.4 meV). It must be stressed, however, that small deviations in the actual $t(E)$ can give rise to large deviations from Eq.(2.18).

For fixed widths of both point contacts (fixed V_{gate}), V_{trans} is found to be quadratic in the current, for $I < 20$ μA [5]. This quadratic dependence is expected for Joule heating. Assuming Joule heating a crude estimate of the electron temperature in the channel can in principle be obtained from a heat balance equation. The generated heat is lost to the lattice, which has a uniform and static temperature T_0, via electron-phonon scattering.

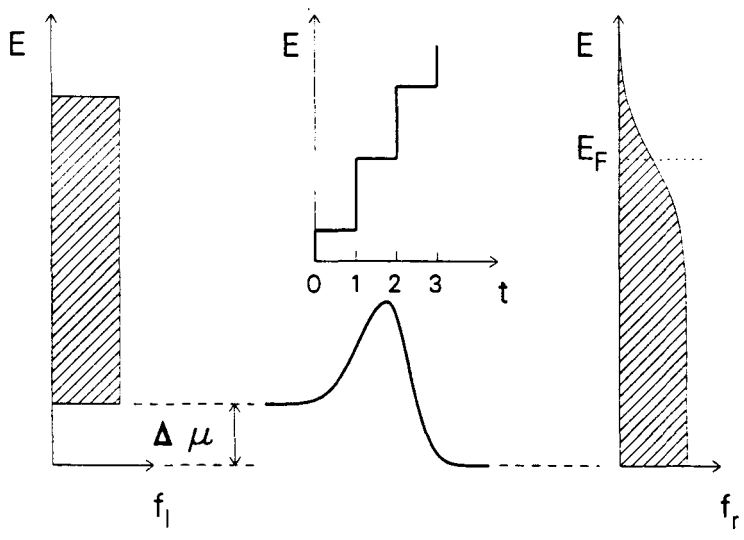

Figure 2.10: Illustration of the origin of the transverse voltage. A cold 2DEG region on the left of the figure is connected via a quantum point contact to the current-heated channel region on the right-hand side. The solid line indicates the bottom of the conduction band in the point contact.

When this is the only heat loss mechanism considered, the heat balance equation is

$$c_{\mathrm{V}}(T - T_0) = \left(\frac{I}{W_0}\right)^2 \rho\tau_{\mathrm{p}} \tag{2.19}$$

where $c_{\mathrm{V}} = (\pi^2/3)(k_{\mathrm{B}}T/E_{\mathrm{F}})n_{\mathrm{s}}k_{\mathrm{B}}$ is the heat capacity per unit area of the 2DEG, $\rho = (n_{\mathrm{s}}e\mu)^{-1}$ is the resistivity in the channel, and τ_{p} the electron-phonon relaxation time. The value of τ_{p} is not accurately known, but the by Leadly *et al.* experimental derived temperature dependent inelastic electron-phonon scattering rate 3×10^8 $\mathrm{s}^{-1}\mathrm{K}^{-1}$ [10] can be used. When also the heat generation at the entrance of the channel is taken into account, which is assumed to be $IR_{\mathrm{pc}}/2$ with R_{pc} the Sharvin resistance of the channel (see Eq.(2.2)), an electron temperature of the same order of magnitude as used in the calculation of Fig. 2.9(b) is obtained from this heat balance [5].

Finally, it is worthwhile noting that the transverse voltage can also be measured if the channel region between the voltage probes carries not net current, *e.g.* if the current is passed through an adjacent point contact. The hot electrons generated at the injecting point contact then distribute their excess energy via rapid electron-electron interactions over the 2DEG channel region. Thus the region between the two voltage probes is heated due to heat conduction in the electron gas.

Chapter 3

Experimental

In this chapter briefly some experimental details are treated concerning the four studies that will be presented separately in the following chapters. The samples used in these studies are processed from the same type of material, and the experiments are all performed in one experimental setup.

3.1 Samples

The samples are fabricated from heterostructure materials grown using MBE at the Philips Research Laboratories in Redhill, England. The heterostructures are of a conventional type and consist of the following layers, which are subsequently grown on top of a semi-insulating substrate: A 1 μm thick GaAs buffer layer, a 40 nm undoped (Al,Ga)As spacer layer, a 40 nm (Al,Ga)As layer doped to 1.3×10^{18} cm^{-3} with Si, and an undoped 20 nm GaAs capping layer. (The spacer thickness of sample G373, however, is 20 nm.) The Al fraction in the (Al,Ga)As layers is 33%.

The modulation doping results in a high mobility 2DEG in the GaAs layer at the (Al,Ga)As–GaAs interface, as is illustrated in the band bending diagram in Fig. 3.1. Conduction electrons from the ionized silicon donors are confined in a triangular potential well at the (Al,Ga)As–GaAs interface. This well is formed by the conduction band offset of about 0.3 eV between the GaAs and the (Al,Ga)As, and the attractive electrostatic potential due to the positively charged ionized donors in the n-doped (Al,Ga)As layer. The spacer layer is introduced to reduce scattering from these donors. Thus, the electron mobility is enlarged. In the triangular well two-dimensional subbands are formed as a result of confinement perpendicular to the interface. In our experiments, both temperature and electron density are such that only one 2D subband is occupied. So we have free two-dimensional electron transport along the (Al,Ga)As–GaAs interface (for a review of semiconductor heterostructures, the formation of 2DEGs, etc. see

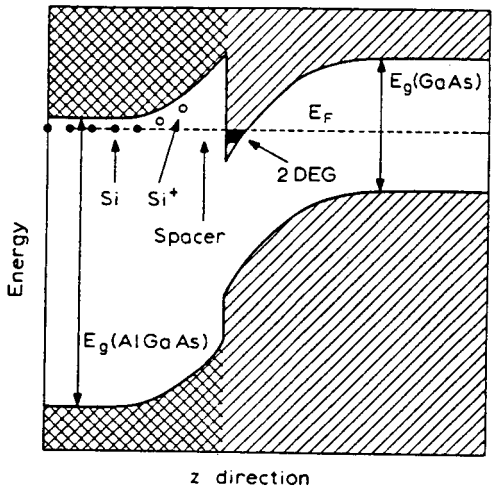

Figure 3.1: Energy scheme of a modulation-doped heterojunction between (Al,Ga)As (with undoped spacer and Si-doped regions) and undoped GaAs. The two- dimensional electron gas (2DEG) is formed at the interface, where the Fermi-level E_F crosses the potential minimum in the conduction band, from Ref.[11].

Ref.[11]).

The top of the heterostructure is mesa-etched in the form of a 1 mm × 0.3 mm Hall bar. Contact to the 2DEG is made by alloyed AuGeNi ohmic contacts, located along the edges of the Hall bar. A pattern of gold gates on the Hall bar is defined by electron-beam lithography, using a double layer PMMA photoresist. As described in Section 2.1, this pattern is imaged in the 2DEG by applying a negative voltage on the gates, that depletes the 2DEG regions under the gates when the voltage exceeds a threshold. The lithographic opening of the split-gates, by which the point contacts are defined, is typically 200 –500 nm.

The electron sheet density, the mobility, and some other related transport parameters of the samples studied in this work are listed in Table 3.1. On the samples* marked with an asterisk experiments were performed after a short period of illumination in the dark. The listed transport parameters concern the sample after illumination. Throughout this report, the electron effective mass is denoted with m, which is for GaAs 0.067 × m_e, with m_e the free electron mass.

3.2 Experimental Set-Up

The measurements were performed with the samples kept in an Oxford Instruments cryostat, which is equipped with a superconducting magnet that can generate a maxi-

		G373 B13	G620 D54	G622 A4*	G627 D9*	G627 D15*	G627 D19*
n_s	(10^{11} cm^{-2})	3.47	2.21	3.32	3.44	3.51	3.36
μ	(10^6 cm^2/Vs)	1.4	1.6	3.1	3.7	3.7	3.7
$k_F = (2\pi n_s)^{1/2}$	(10^6 cm^{-1})	1.48	1.18	1.44	1.47	1.49	1.45
$v_F = \hbar k_F/m$	(10^7 cm/s)	2.6	2.0	2.5	2.5	2.6	2.5
$E_F = (\hbar k_F)^2/2m$	(meV)	12	7.9	12	12	13	12
$l_e = v_F\tau = v_F m\mu/e$	(μm)	14	12	30	35	37	35

Table 3.1: Some transport parameters of the samples used in this work.

mum magnetic field perpendicular to the sample of $B_{max} = 10$ T. Unless stated otherwise, the sample temperature during the measurement is $T = 1.7$ K, which is reached during normal operation of the cryostat while pumping down a small helium reservoir that surrounds the sample chamber. The sample temperature is measured with a Lake Shore Cryotronics carbon glass resistor, and the magnetic field is determined by measuring the current through the superconducting magnet (magnetic field to current ratio is 0.145 T/A). Care was taken to minimize hysteresis effects in magnetic field scans.

The measurements are controlled by a HP Vectra ES/12 personal computer using Asystant GPIB software. A Philips PM 5168 function generator and a Philips PM 5180 attenuator are used to generate a low amplitude (100-500 μV RMS) low frequency (12 Hz) ac excitation signal. Two EG&G Princeton Applied Research model 5204 lock-in analyzers are used for detection of the ac signals. For the generation of ac and dc voltages and currents, a two-channel HP 3245A universal source is available. In addition, a four channel HP 6626A dc power supply is sometimes used to generate dc voltages. dc Voltages are measured with an eight-channel HP 3457A multimeter. An Oxford Instruments power supply 2127, that generates the current through the superconducting magnet, is controlled via a Keithley 230 programmable voltage source.

Although also straightforward dc measurements are performed, the standard measurement technique is the low frequency ac double lock-in method, which is illustrated in Fig. 3.2. A 12 Hz ac current, generated by a low amplitude excitation voltage (100 μV RMS, to prevent electron heating), is passed through the sample and an adjustable reference resistance. With two lock-in amplifiers the ac voltage drops over both the sample and the series resistance are detected. The sample resistance is then given by $R_{sample} = R_{ref}(V_{sample}/V_{ref})$; obviously the excitation current drops out of this expression. It must be noted that the current and voltage contacts on the sample need not be the

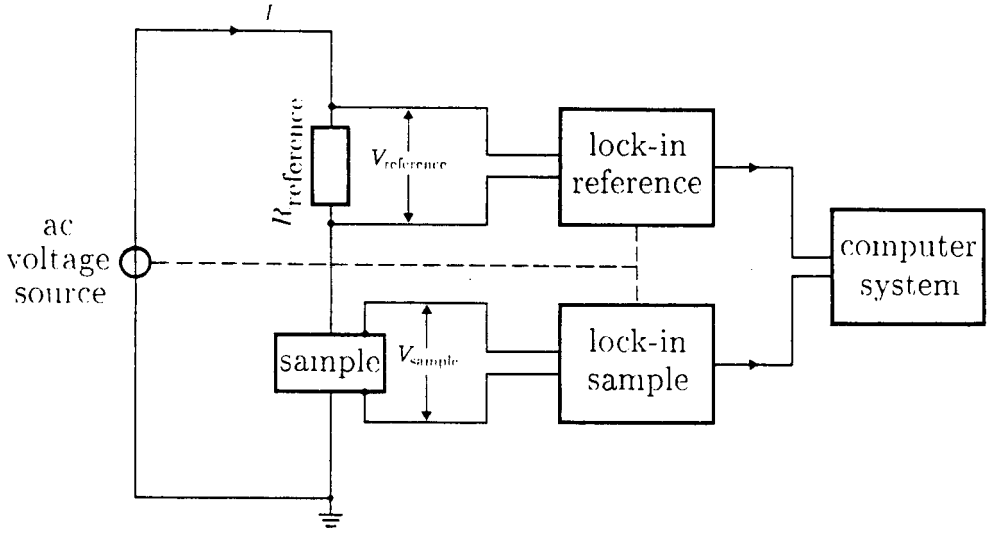

Figure 3.2: Schematic ac double lock-in measurement technique.

same (*e.g.* in a Hall measurement). When a current flows from contact 1 to contact 2 and the voltage is measured between contacts 3 and 4, the sample resistance is denoted as $R_{12,34} \equiv V_3 - V_4/I$. If a dc bias is added to the ac excitation signal, the double lock-in technique yields a differential sample resistance $\mathrm{d}V/\mathrm{d}I$ at that bias.

Chapter 4

Electrostatic Manipulation of an Electron Beam

4.1 Introduction

In an industrial research laboratory an obvious question raised by the electron beam collimation experiment (Section 2.3) is, whether these electron beams can be manipulated in such a way that, *e.g.* an electron beam switch in principle is possible. In the experiment of Ref.[7] the injected collimated beam was swept past the collector using a magnetic field, which is clearly not usable in a nanostructure switch device meant for mass application.

In this chapter we will concentrate on electrostatic electron beam manipulation, *i.e.*, by applying different voltages on the different parts of the split gates that define the point contacts in the 2DEG. Glazman and Larkin [12] have calculated that the confining potential of a split gate induced constriction in a 2DEG can be shifted laterally with little change in shape, by applying different voltages on the split gate halves. Recently, Williamson *et al.*[13] used this method to study the local potential in the 2DEG. We have studied electrostatic electron beam manipulation in two different point contact geometries. A 'slit' point contact in between injecting and collecting point contacts was used to affect the line of sight between injector and detector in both configurations. The chapter is concluded with a rather remarkable result, which was accidentally obtained from another sample.

4.2 Point Contacts as Movable Electron Slits

Three quantum point contacts in series, with 4 μm distance between adjacent point contacts, were used as injecting, 'slit', and collecting point contacts respectively. The

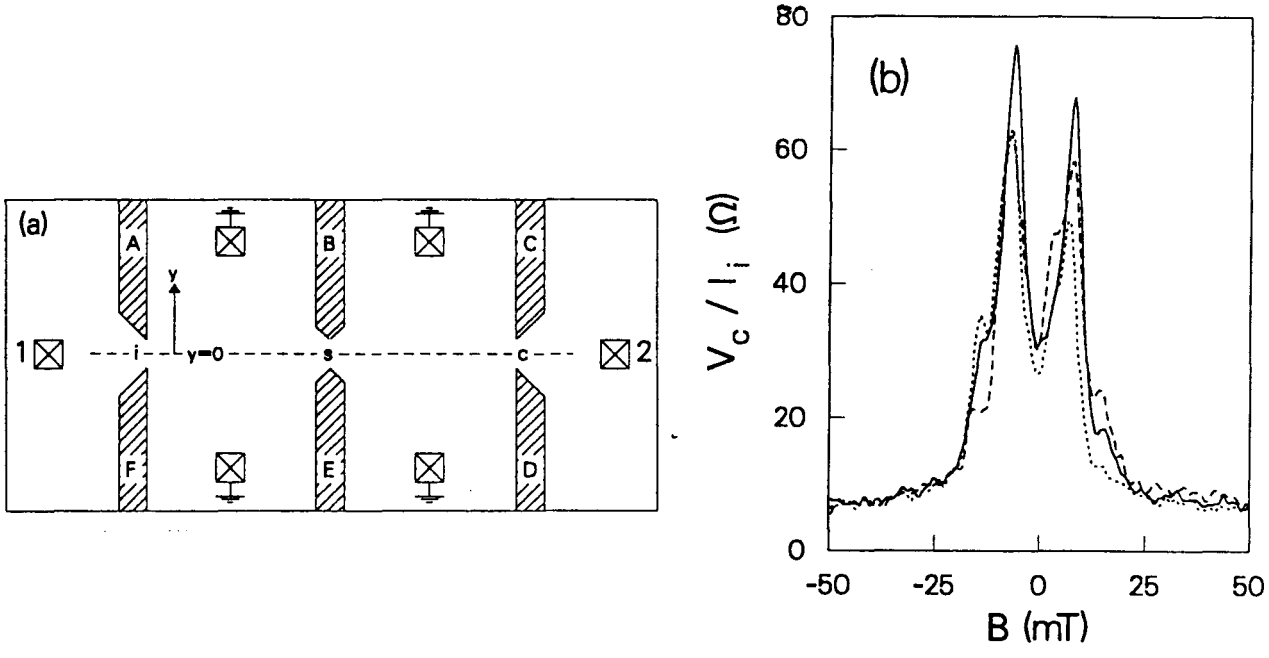

Figure 4.1: (a) Lay out of sample G622A4, with three point contacts in series aligned along the dashed line. Hatched areas denote the gates and Ohmic contacts to the 2DEG are represented by crosses. The distance between adjacent point contacts is 4 μm. (b) Collimation signal as function of magnetic field, with all point contacts set to $N = 3$ and point contacts i and c defined by symmetric gate voltages. Gate voltages on gates B and E were such that point contact s was centered around $y = 0$ (solid line), shifted in positive y-direction (dashed), or shifted in negative y-direction (dotted).

results presented in this section were obtained from sample G622A4, whose lay out is schematically drawn in Fig. 4.1(a), and for which some transport parameters are listed in Table 3.1. A 12 Hz 100 μV ac excitation voltage was applied between Ohmic contact 1 and a grounded contact, giving rise to a ballistic electron beam injected through point contact i. The ballistic electrons collected by point contact c are detected by measuring the voltage of Ohmic contact 2 (relative to a grounded contact), using the standard double lock-in method (Section 3.2). (Note that, due to the ac measurement technique, injector and collector are interchangeable.) Only ballistic electrons that travel directly through the three point contacts contribute to the collector voltage V_c, because scattered electrons are drained to ground in the intermediate 2DEG regions.

The lithographic openings are aligned around the dashed line in Fig. 4.1(a), so that at zero magnetic field and symmetric point contact gate voltages the collimation signal V_c/I_i should be at a maximum. We can use voltage differences between the split gate halves of the three point contacts to scan the electrostatic openings in the y-direction [12,13]. In Fig. 4.1(b) magnetic field scans of the collimation signal are presented. For

all curves the gate voltages were such that three 1D subbands were populated in all three point contacts ($N = 3$). The injector point contact i and collector point contact c both were defined by symmetric gate voltages. The solid curve was obtained for a symmetric gate voltage defining point contact s, $V_{\rm gate}^{\rm BE}$=–1.71 V. The center point contact s was shifted in positive y-direction for the dashed curve, $V_{\rm gate}^{\rm B}$=–1.26 V and $V_{\rm gate}^{\rm E}$=–2.16 V, and shifted in the negative y-direction for the dotted curve, $V_{\rm gate}^{\rm B}$=–2.15 V and $V_{\rm gate}^{\rm E}$=–1.26 V. The most striking feature of Fig. 4.1(b) is that two collimation peaks are observed, whereas a single collimation peak centered around $B = 0$ is expected (Section 2.3). A collimation pattern similar to Fig. 4.1(b) was obtained from another magnetic field scan of the collimation signal (not shown here), using point contacts s and c as injector and collector, while a major peak at $B = 0$ with some side peaks was observed using i and s as injector and collector.

The striking similarity of the pattern in Fig. 4.1(b) to a Fresnel diffraction pattern in optics directly suggests an interpretation in terms of scattering of the electron waves by an impurity, close to either injector or collector. We believe indeed that this interpretation is correct, since for the point contact resistances used, we have a quite coherent electron source. For N 1D subbands occupied in the injecting point contact, the electrons are injected in N independent modes. Interference effects average out for $N \gg 1$ modes, but are resolved for $N = 3$. The exact collimation diffraction pattern is well reproducible during one cool-down, but is often altered significantly after thermal cycling of the sample. We therefore contribute structure additional to a single collimation peak at $B = 0$ to diffraction of the ballistic electrons by impurities, which is best resolved for small N. Apparently in the experiment of Fig. 4.1(b) the impurity configuration in between point contacts s and c partly blocked detection of ballistic electrons at $y = 0$.

Shifting point contact s slightly decreases the height of the two major peaks and slightly changes the impurity diffraction pattern, but does not reveal any dramatic effects. Note that the positive background in Fig. 4.1(b) is part of the Ohmic resistance of the contact used as reference for $V_{\rm c}$, because at that contact part of $I_{\rm i}$ is drained to ground.

The maximum effect in the collimation signal at zero magnetic field is expected for shifting all three point contacts at the same time, with point contact s shifted in opposite direction as point contacts i and c. Let us define a gate voltage difference $\Delta V_{\rm gate} = V_{\rm gate}^{\rm A}$–$V_{\rm gate}^{\rm F} = V_{\rm gate}^{\rm E}$–$V_{\rm gate}^{\rm B} = V_{\rm gate}^{\rm C}$–$V_{\rm gate}^{\rm D}$, so that for $\Delta V_{\rm gate}$>0 V point contacts i and c are shifted in positive y-direction and point contact s in negative y-direction. In Fig. 4.2 the zero-field collimation signal is shown as function of $\Delta V_{\rm gate}$, obtained on another cool-down of sample G622A4, after temperature cycling overnight to 50 K after the experiment of Fig. 4.1(b). Average gate voltages were applied such that all point contacts were set to $N = 2$: $\overline{V}_{\rm gate}^{\rm AF} = \frac{1}{2}(V_{\rm gate}^{\rm A}+V_{\rm gate}^{\rm F})$ = –2.62 V, $\overline{V}_{\rm gate}^{\rm BE}$ = –1.83 V, and $\overline{V}_{\rm gate}^{\rm CD}$

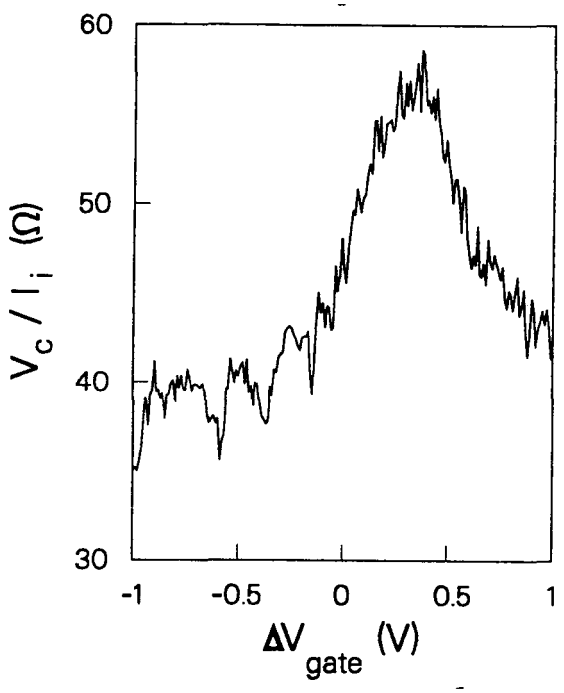

Figure 4.2: Zero-field collimation signal as function of ΔV_{gate}, which is defined in the text. Scanning ΔV_{gate} from −1 V to +1 V corresponds to shifting point contacts i and c from negative y to positive y, and shifting point contact s from positive y to negative y. The average gate voltages are such that all quantum point contacts are set to $N = 2$. (Sample G622A4).

= −2.70 V. The resistances of the three point contacts were observed to vary less than 10% from $R = h/4e^2$ for $-1.0 \leq \Delta V_{\text{gate}} \leq 1.0$V. Scanning ΔV_{gate} indeed yields a peak in the zero-field collimation signal, although the signal is very small. The peak is not centered at ΔV_{gate}=0, as would be expected, which may be due to a slight misalignment of the lithographic gate pattern, or to a small reminiscent magnetic field in the cryostat. The larger background resistance than observed in Fig. 4.1(b) may be due to the fact that V_c was measured relative to a different grounded contact.

The result of Fig. 4.2 can be compared to a simple calculation of the overlapping of the openings of the three point contacts in the y-direction. Because all the point contacts are set to $N = 2$, we assume that the electrostatic openings of the point contacts in the 2DEG, W_{min}, equal the Fermi wave length $\lambda_F = 2\pi/k_F$, yielding $W_{\text{min}} = 44$ nm (see Table 3.1). The lateral position of the potential minimum between two infinitely long colinear wires at voltages V_1 and V_2 separated by an opening W is

$$y_{\text{min}} = \frac{W}{2}\frac{V_1 - V_2}{V_1 + V_2} \tag{4.1}$$

Using Eq.(4.1) point contacts i and c can be represented as openings from y_b to y_t, given

by

$$y_b = -\frac{W_{min}}{2} - \frac{W}{4}\frac{\Delta V_{gate}}{\overline{V}_{gate}} \; ; \qquad y_t = +\frac{W_{min}}{2} - \frac{W}{4}\frac{\Delta V_{gate}}{\overline{V}_{gate}} \tag{4.2}$$

whereas point contact s forms an opening between

$$y_b = -\frac{W_{min}}{2} + \frac{W}{4}\frac{\Delta V_{gate}}{\overline{V}_{gate}} \; ; \qquad y_t = +\frac{W_{min}}{2} + \frac{W}{4}\frac{\Delta V_{gate}}{\overline{V}_{gate}} \tag{4.3}$$

Here W is the lithographic opening of the point contact. Because the positions of the openings are linearly in ΔV_{gate}, we expect a triangular collimation signal as function of ΔV_{gate}, with maximum at ΔV_{gate}=0 V. The width of the triangular peak can be estimated from the condition that the signal vanishes when there is no line of sight through the three openings. Because point contact i and c are virtually the same, *i.e.* exhibit virtually identical resistances as function of gate voltage, the collimation signal should vanish for ΔV_{gate} such that $y_t^i = y_b^s$:

$$\frac{1}{4}\left(\frac{W^{AF}}{\overline{V}^{AF}} + \frac{W^{BE}}{\overline{V}^{BE}}\right)\Delta V_{gate} = -W_{min} \tag{4.4}$$

Using the split gate openings $W^{AF} = 440$ nm and $W^{BE} = 320$ nm, the full width of the collimation peak is calculated as $2\Delta V_{gate} = 1.0$ V. This calculated width is of the same order of magnitude as the width observed in Fig. 4.2. The smaller experimental width also indicates a small misalignment or reminiscent magnetic field.

4.3 Impurity Effects Governing the Electron Beam Manipulation

The small signal of Fig. 4.2 prohibits collimated electron beam manipulation in a sufficient controlled way. Because for the line of sight type experiments only the injector to 'slit' distance must be large compared to the openings of the point contacts, the collimation signal can be increased by locating the collector just behind the 'slit' point contact. Therefore we have designed a sample with similar lay out as given in Fig. 4.1(a), with 3.3 μm distance between point contacts i and s, and 0.8 μm distance between point contacts s and c (leaving a lithographic opening of 0.4 μm between the gates defining s and c). The results presented below were obtained from sample G627D9, for which some transport parameters are given in Table 3.1. Average gate voltages were applied such that in all three quantum point contacts one 1D subband was populated ($N = 1$). The zero-field collimation signal V_c/I_i was monitored as function of a gate voltage difference ΔV_{gate} on all split gates. The point contact resistances were observed to vary less than 10% from $R = h/2e^2$ for $-0.6 \leq \Delta V_{gate} \leq 0.6$V. The results of scanning ΔV_{gate} in four

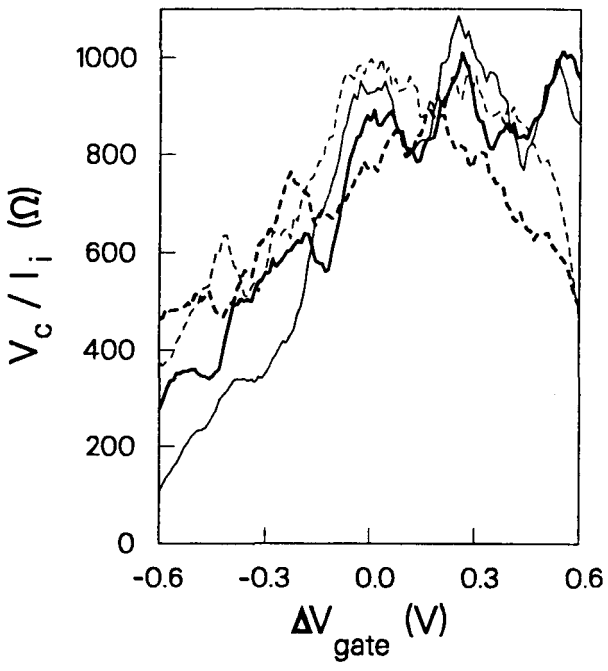

Figure 4.3: Zero-field collimation signal as function of gate voltage difference $\Delta V_{\rm gate}$ on the split gates defining all three point contacts. Solid lines correspond to scanning center point contact s in opposite direction as the scanning direction of point contacts i and c, whereas the dashed lines correspond to scanning all three point contacts laterally in the same direction. Thick curves are obtained from a scan from left to right, and thin curves result from a scan from right to left. All point contacts were set to $N = 1$ for all $\Delta V_{\rm gate}$. (Sample G627D9).

different ways are presented in Fig. 4.3. Assume the same labelling of gates as used in Fig. 4.1(a). The solid curves in Fig. 4.3 represent the same experiment as presented in Fig. 4.2, *i.e.* $\Delta V_{\rm gate}$ defined as $\Delta V_{\rm gate} = V^{\rm A}_{\rm gate}-V^{\rm F}_{\rm gate} = V^{\rm E}_{\rm gate}-V^{\rm B}_{\rm gate} = V^{\rm C}_{\rm gate}-V^{\rm D}_{\rm gate}$, so that point contact s is scanned in opposite direction as point contacts i and c. For the dashed lines, $\Delta V_{\rm gate}$ is given by $\Delta V_{\rm gate} = V^{\rm A}_{\rm gate}-V^{\rm F}_{\rm gate} = V^{\rm B}_{\rm gate}-V^{\rm E}_{\rm gate} = V^{\rm C}_{\rm gate}-V^{\rm D}_{\rm gate}$, so that the dashed lines represent the collimation signal when all three point contacts are scanned in the same direction. Furthermore, the thick lines correspond to scanning of $\Delta V_{\rm gate}$ in positive direction, -0.6 V $\rightarrow$ $+0.6$ V, whereas the thin lines were obtained from scanning $\Delta V_{\rm gate}$ in the negative direction, $+0.6$ V $\rightarrow$ -0.6 V. The experimental traces were obtained from a single scan, but reproduced well during one cool-down of the sample.

As shown in Fig. 4.3 the collimation signal is indeed much larger than that of Fig. 4.2, where the injector–collector distance was twice as large. The collimation signal varies significantly upon scanning $\Delta V_{\rm gate}$. However, the exact behavior of $V_{\rm c}/I_{\rm i}$ *vs.* $\Delta V_{\rm gate}$ depends on the scan direction, for reasons presently unknown. Furthermore,

there is no striking difference between scanning the center point contact s in the opposite direction or in the same direction as injecting and detecting point contacts. Apparently, impurity diffraction close to i and c governs the collimation signal. By varying ΔV_{gate} the diffraction pattern is scanned, which affects the collimation signal stronger than the change in overlap of the openings in the y-direction. The single mode operation of the quantum point contacts ($N = 1$) and the small lithografic widths of the point contacts (0.2 μm) may partly be responsible for the observation of mainly impurity diffraction effects instead of 'line of sight' effects.

Electrostatic beam manipulation was also attempted by using the two closely separated point contacts c and s of sample G627D9 as an injecting orifice, and using point contact i as detector. Steering of the injected beam was attempted by applying gate voltage differences on the split gates defining c and s, thereby attempting to create a controllable asymmetric injecting orifice. However, these experiments did not reveal any evidence for controlled manipulation of the angle of the injected collimated electron beam.

4.4 Conclusion

We have seen in Section 4.2 that the line of sight between three point contacts in series can be affected by shifting the point contacts in lateral direction. The zero-field collimation signal in sample G622A4 was, however, too small for sufficient controllable electron beam manipulation. The large collimation signal of sample G627D9 in Section 4.3 severely suffered from impurity diffraction. These effects could probably be partly suppressed by using point contacts at $N \gg 1$, which have larger lithographic openings. However, we think that manipulation of collimated electron beams is very difficult to preform at a controlled level by lateral shifting the involved point contacts.

After having finished our attempts to electrostatic electron beam manipulation, we, more ore less accidentally, obtained a remarkable result while studying electron–electron interactions in the ballistic regime (see Chapter 7). In Fig. 4.4(a) the sample lay out of sample G627D19 is presented. Using the standard low amplitude low frequency double lock-in technique, a normal collimation experiment was performed by measuring the collimation signal $V_{\text{c}}/I_{\text{i}} = R_{23,14}$ as function of the magnetic field. Average gate voltages were applied to the split gates defining point contacts i and c such that both point contacts were set to $N = 1$. In Fig. 4.4 the results are shown for two magnetic field scans for the same (symmetric) voltage on the gates defining point contact i. The drawn curve corresponds to a magnetic field scan with symmetric gate voltages on the gates defining point contact i. A large collimation peak at $B = 0$ is observed, accompanied by

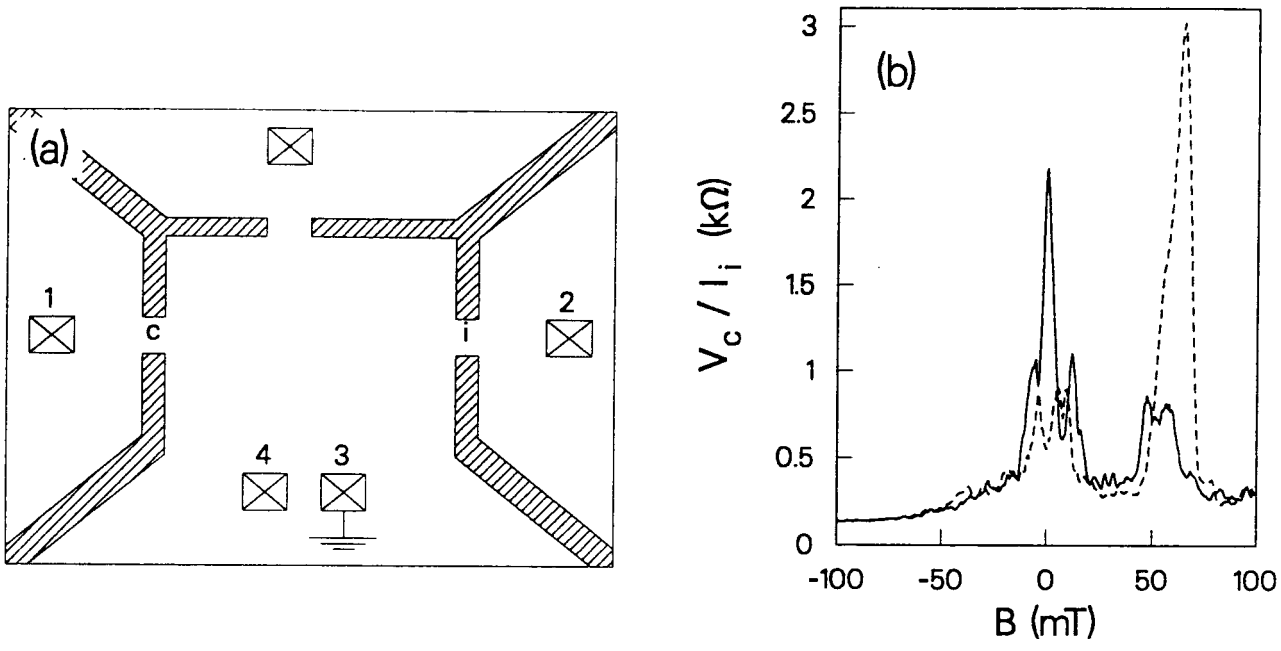

Figure 4.4: (a) Lay out of sample G627D19. Hatched areas denote the gates and Ohmic contacts to the 2DEG are represented by crosses. (b) Magnetic field scans of the collimation signal of sample G627D19, with injecting and collecting point contacts set to $N = 1$. The solid curve was obtained for symmetric gate voltages defining point contact i, and the dashed line resulted from asymmetric gate voltages defining point contact i.

some impurity diffraction peaks ($N = 1$), and a smaller peak at $B = 0.06$ T is obtained from ballistic electrons reaching collector c after bouncing once at the horizontal part of the upper right gate, see Fig. 4.4(a). (Note that the upper point contact is not centered between i and c, but is closer to point contact c.) The dashed curve of Fig. 4.4(b) was obtained for a gate voltage difference of 0.83 V between the gates defining point contact i (the lower gate having the largest negative potential). This lateral shift of point contact i, in vertical upwards direction in Fig. 4.4(a), has a large effect on the collimation signal. The central peak at $B = 0$ is suppressed to a large extent, whereas the 'bouncing' peak is increased enormously. These effects could be due to an accidental strongly varying impurity potential near point contact i. The change in the collimation signal at $B = 0.06$ T might also somehow be due to the different voltage on the upper right gate, on which the bouncing takes place. A different voltage on that gate causes a slightly different distance of the 'bouncing' potential wall to the line interconnecting injector and collector. Although we have not further studied these effects, Fig. 4.4 suggests that there might be some interesting unrevealed effects.

Chapter 5

Thermal Conductance of a Quantum Point Contact

5.1 Introduction

As discussed in Chapter 2, quantum effects have been observed so far in the electrical conductance G and the thermopower S of quantum point contacts. As was shown by Butcher [8], the other global transport coefficients, the thermal conductance κ and the Peltier coefficient Π, should also exhibit quantum effects. The thermal conductance, upon which we will concentrate in this chapter, is related to the electrical conductance by the Wiedemann-Franz law, which for a point contact with conductance G is written as [8]

$$\frac{\kappa}{GT} = L_0 \tag{5.1}$$

Here L_0 is the Lorentz number, which is for a degenerate gas given by $L_0 = (\pi k_B/e)^2/3$. Thus κ of a point contact should show the same staircase behavior as G, for a fixed temperature T.

5.2 Experimental

In Fig. 5.1 the lay-out of the sample designed for thermal conductance measurements is shown. A low frequency ($f = 12$ Hz) ac current is passed from contact 2 to contact 3, where the current is drained to ground, thereby selectively heating the 2DEG in the narrow channel region (with lithographic width $W_{ch} = 0.4$ μm and length $L_{ch} = 3$ μm). We assume that the Joule dissipation only heats the electron gas, and that the lattice remains at uniform temperature T_0 due to the weak electron–phonon coupling, see Section 2.4. The thermal conductance of point contact m can now in principle be measured by detecting the electron temperature in the bath region (which has three

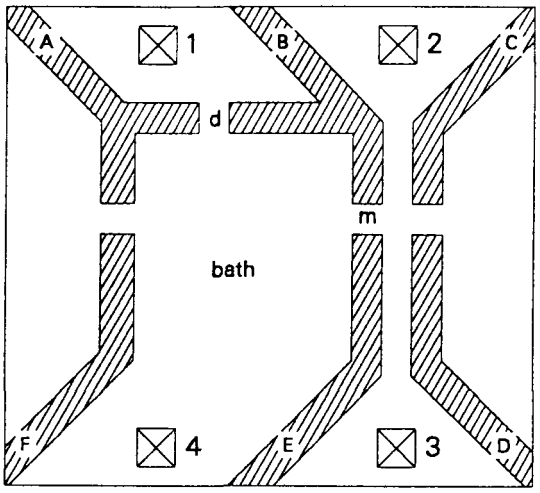

Figure 5.1: Lay out of the sample for thermal conductance measurements. Gates are indicated as hatched areas and crosses refer to Ohmic contacts to the 2DEG.

3 μm long boundaries and one open side that leads to Ohmic contact 4), as function of the width of point contact m. Although we can not directly measure the electron temperature, the thermopower of a quantum point contact can be used to monitor the electron temperature, see Section 2.4. The thermovoltage over detection point contact d, $V_{\rm thermo} = V_4 - V_1$, is proportional to the electron temperature difference between the bath, which is modestly heated by heat flowing through point contact m, and the cold 2DEG region of contact 1, which is at lattice temperature T_0.

As shown by Molenkamp *et al.*[5], the thermovoltage of a point contact in a 4 μm wide channel is quadratic in the current through the channel up to 20 μA. Thus we assume that the electron temperature in the 0.2–0.3 μm wide channel (electrostatic width in the 2DEG) in our samples is quadratic in the current up to at least 1 μA. For these low current levels, the ac channel current $I = \hat{I}\cos\omega t$ gives rise to a thermovoltage over point contact d, $V_{\rm thermo} = \frac{1}{2}cI^2 = c(\hat{I}\cos\omega t)^2 = \frac{1}{2}c\hat{I}^2(\cos 2\omega t + 1)$, where c is a constant with dimension (V/A^2). Thus the ac current with frequency $f = 12$ Hz yields a thermovoltage with frequency $2f = 24$ Hz, which can selectively be detected using a lock-in amplifier in the second-harmonic detection mode. It must be noted that the detected second-harmonic signal has root-mean-square value $V_{\rm det}^{\rm rms} = \frac{1}{\pi}c\hat{I}^2$ that differs from the expected thermovoltage $V_{\rm thermo}^{\rm rms} = c(I^{\rm rms})^2 = c(\frac{2}{\pi}\hat{I})^2$. Therefore we have calculated the thermovoltage from the detected second-harmonic signals as $V_{\rm thermo}^{\rm rms} = \frac{4}{\pi}V_{\rm det}^{\rm rms} = \frac{4}{\pi}(V_4 - V_1)_{\rm det}^{\rm rms}$.

5.3 Quantized Thermal Conductance

The results presented in this Section were obtained from sample G627D15, for which some transport parameters are listed in Table 3.1. A gate voltage of $V_{\rm gate}^{\rm BCDF} = -1.15$ V was applied to the gates B, C, D, and F, see Fig. 5.1. The electrical conductance of point contact m was obtained as a function of the voltage on gate E, using the low frequency low amplitude double lock-in technique described in Section 3.2. Then a fixed ac current ($f = 12$ Hz) through the channel was applied and $V_{\rm gate}^{\rm A}$ was adjusted such that the thermovoltage signal $V_{\rm thermo}^{\rm rms}$ at $f = 24$ Hz was at a maximum value, corresponding to a setting of point contact d between $N = 1$ and $N = 2$ ($V_{\rm gate}^{\rm A} \approx -1.4$ V). A small magnetic field of 15 mT was applied perpendicular to the sample (with direction upwards in Fig. 5.1), to avoid direct detection of hot electrons travelling ballistically from point contact m to point contact d.

In Fig. 5.2 the quantized electrical conductance of point contact m is shown (dashed line) as function of $V_{\rm gate}^{\rm E}$. In the same figure also the thermovoltage $V_{\rm thermo}^{\rm rms}$ over point contact d as function of $V_{\rm gate}^{\rm E}$ is given (solid line) for an ac current $I^{\rm rms} = 0.57$ μA and sample temperature $T_0 = 1.38$ K. This figure clearly shows a stepwise thermovoltage over point contact d that lines up with the electrical conductance of point contact m, implying a *quantized thermal conductance* of point contact m.

The results of the same experiment obtained from a different cool-down are shown in Fig. 5.3. The dashed line depicts the electrical conductance of point contact m, and the solid lines represent the thermovoltage of point contact d for different ac currents through the channel, as function of $V_{\rm gate}^{\rm E}$. The subsequent thermovoltage traces were obtained for ac currents $I^{\rm rms}$ =0.29 μA, 0.43 μA, 0.57 μA, and 0.72 μA, respectively, all at sample temperature $T_0 = 1.68$K. The quantized structure in $V_{\rm thermo}^{\rm rms}$ remains observable up to the highest current level. The thermovoltage is in good approximation quadratic in the current, as follows from Fig. 5.3 (except for the lowest current level) and from other experiments (not shown here), which implies that $V_{\rm thermo}^{\rm rms}$ indeed arises from second harmonic detection at $2f$, and is not caused by any spurious f signal.

5.4 Conclusion

We have observed for the fist time the quantized thermal conductance of a quantum point contact, that resembles the electrical conductance quantization, as was expected from the Wiedemann-Franz law (Eq.(5.1)). Quantitatively, we have tried to compare the thermal conductance κ as calculated from this Wiedemann-Franz law with the κ

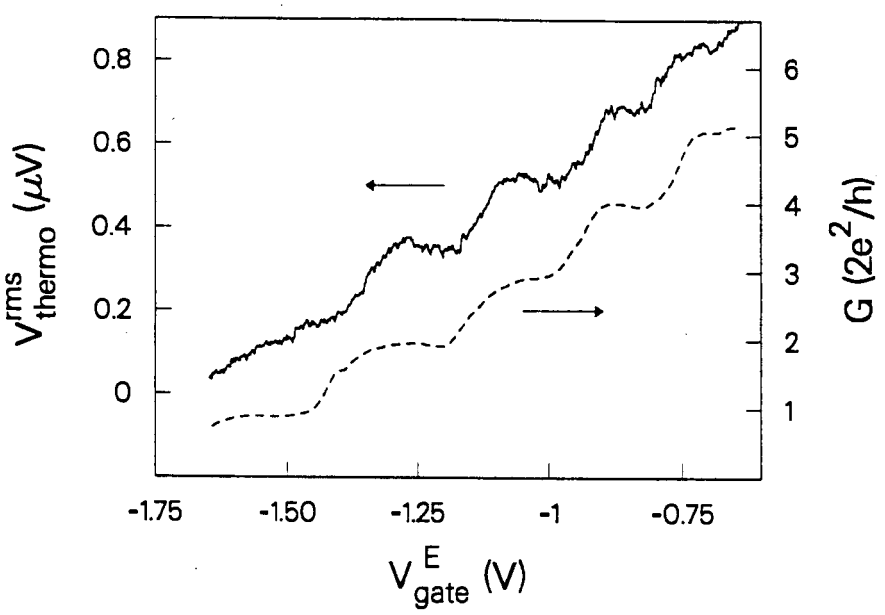

Figure 5.2: Electrical conductance (dashed curve) of point contact m (corrected for background resistance), and thermovoltage (solid curve) of point contact d, as function of the voltage on gate E, the other gate voltages being fixed. The thermovoltage shows a quantized behavior similar to G of point contact m, which is interpreted as a quantized thermal conductance of point contact m. (Sample G627D15).

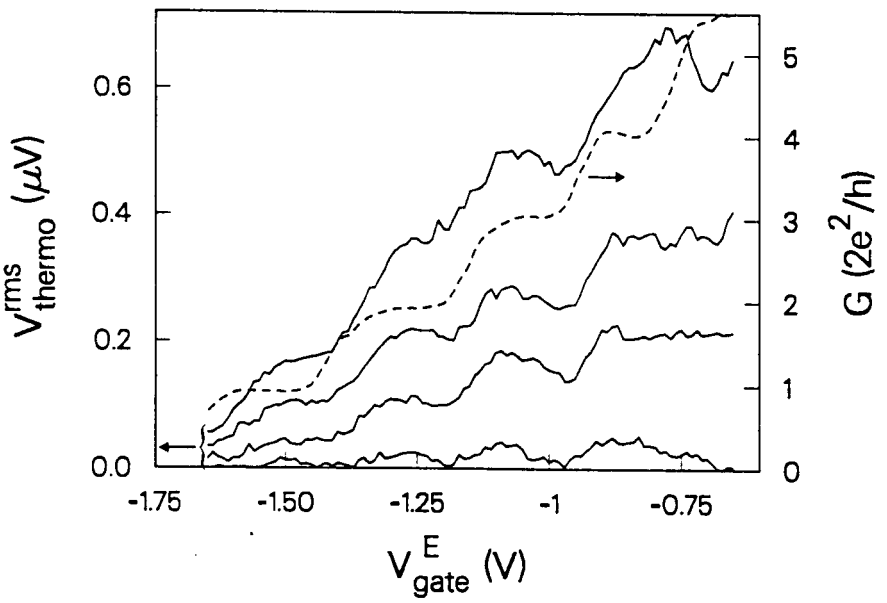

Figure 5.3: Thermovoltage signal (solid lines) arising from the quantized thermal conductance of point contact m, compared to the electrical conductance of m (dashed). The subsequent thermovoltage traces (bottom to top) were obtained for I^{rms} =0.29 μA, 0.43 μA, 0.57 μA, and 0.72 μA through the channel respectively, all at sample temperature $T_0 = 1.68$K.

calculated from a very simplified heat-balance equation for the bath region:

$$\kappa\,(T_{\rm ch} - T_{\rm bath}) = \frac{1}{\tau_{\rm p}}\, c_{\rm v} A_{\rm bath}\,(T_{\rm bath} - T_{\rm T_0}) \tag{5.2}$$

with $\tau_{\rm p}$ the electron-phonon relaxation time [10], $c_{\rm v} = (\pi^2/3)(k_{\rm B}T_{\rm bath}/E_{\rm F})n_{\rm s}k_{\rm B}$ the heat capacity per unit area of the 2DEG bath region, and $A_{\rm bath}$ the area of the bath region (assumed 3 μm $\times$ 3 μm). However, to yield the same order of magnitude for κ as calculated from the Wiedemann-Franz law, a much lower channel temperature $T_{\rm ch}$ has to be inserted in Eq.(5.2) than expected from channel heating experiments at similar current density levels in a 4 μm wide channel [5]. This may be due to the strong anisotropic heating of the bath region in the experiment, while Eq.(5.2) assumes an isotropic distribution of the heat in the bath region, and/or the not accurately known and probably electron temperature dependent value of $\tau_{\rm p}$. A better quantitative understanding of thermal effects in a 2DEG can be obtained when the proportionality factor between the thermovoltage of a point contact and electron temperature difference could be determined for the point contacts used in the experiments. Then the quantum point contacts can be used as absolute thermometers of the local electron temperature difference between two 2DEG regions.

Chapter 6

Voltage Probe Controlled Breakdown of the Quantum Hall Effect

6.1 Introduction

As discussed in Section 2.2, a high magnetic field gives rise to quasi one-dimensional extended states, called edge channels, at the 2DEG boundaries. Current flowing between two (current) contacts in the 2DEG is, in the linear response regime, carried by the edge states at the Fermi-level, and can be discussed in a natural fashion using the Landauer-Büttiker formalism [14]. Each quasi one-dimensional channel carries the same amount of current $(2e/h)\delta\mu$ (assume spin degeneracy), where $\delta\mu$ is the chemical potential difference between the current contacts. As illustrated in Fig. 6.1, one edge has a high chemical potential $E_{\rm F} + \delta\mu$ and the opposite edge is at low chemical potential $E_{\rm F}$. If N edge states are populated, *i.e.* if the Fermi-level lies in between two Landau levels in the bulk (see Fig. 2.5), the longitudinal resistance vanishes, $R_{\rm L} = 0$, and the Hall resistance has the quantized value $R_{\rm H} = h/2e^2N$, see Fig. 6.1.

The arguments above assume *ideal* contacts. An ideal contact fully transmits all incoming and outgoing edge channels, and distributes the current equally over the edge channels. This implies that non-equally populated incoming edge channels are equilibrated in such an ideal contact, so that the outgoing edge channels are equally populated. Quantum point contacts are essentially non-ideal in this sense, because they can selectively populate and detect the quasi-one dimensional edge channels [14]. In fact, our understanding of the quantum Hall effect has gained considerably as a result of the ability to control the selective transmission of edge channels through point contacts [3,4]. The first experiments of this type involved what is now called the anomalous in-

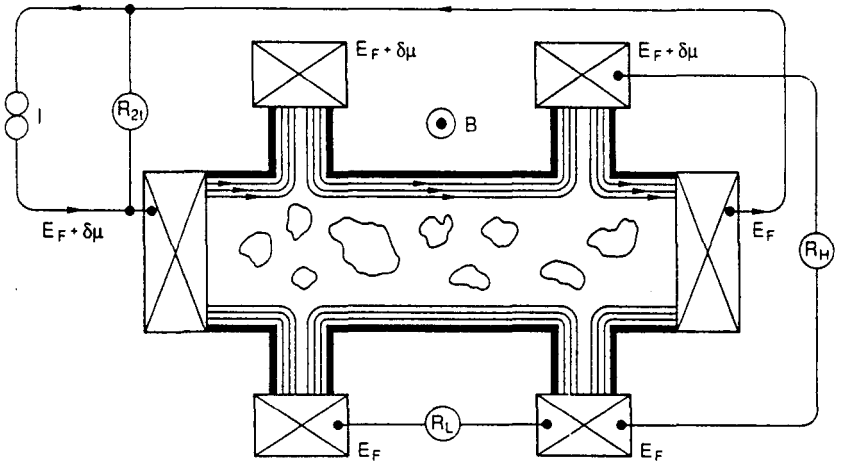

Figure 6.1: Measurement configuration for the four-terminal Hall resistance $R_{\rm H}$ and the longitudinal resistance $R_{\rm L}$. The edge channels at the Fermi level are indicated, arrows point in the direction of motion of edge channels filled by the source contact at chemical potential $E_{\rm F}+\delta\mu$. The current is equipartitioned among the edge channels at the upper edge. Current and voltage contacts are ideal contacts.

teger quantum Hall effect, in which the absence of scattering between the edge channels on the same edge was demonstrated on both microscopic [15] and macroscopic [16,17] length scales. In addition, similar experiments on the longitudinal resistance [18] have provided evidence that backscattering, manifested by Shubnikov-de Haas oscillations, occurs predominantly within the highest occupied Landau level. These, and other [3,4], phenomena observed in the linear response regime of vanishingly small current can be well understood on the basis of Büttiker's model of the quantum Hall effect [14].

The breakdown of the quantum Hall effect at high current densities (the regime of non-linear response) is considerably less well understood. Experimentally [19,20] the breakdown is usually studied in a narrow ($\sim$ 1 μm) channel or constriction. A non-zero longitudinal resistance is observed at large Hall fields, which can be generated at moderate current levels ($\sim$ 0.1 – 1 μA) in such structures. Note that, in a measurement configuration with ideal current contacts, the only possible mechanism for a non-zero longitudinal resistance is backscattering between two edge states at opposite edges. Several mechanisms have been proposed (*cf.* Ref. [21] and references therein), but the interpretation of the experiments is not unambiguous. In this chapter we report results of an experimental study of the breakdown of the quantum Hall effect in a novel geometry, *i.e.* a narrow channel fitted with adjustable point contact voltage probes. We use the voltage probes to adjust the *equilibration* of the highest occupied Landau level with the lower levels. Our data provide evidence that breakdown occurs predominantly through selective backscattering of electrons in the highest Landau level. The study

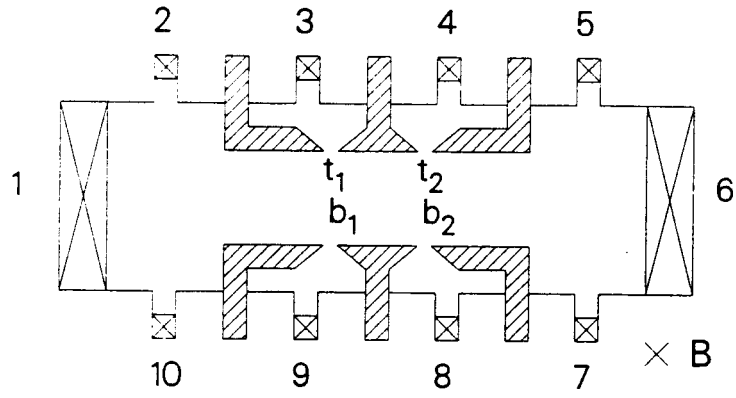

Figure 6.2: Lay-out of sample G373B13 (not to scale), containing a narrow channel (of width 4 μm and length 18 μm) with point contact voltage probes (3 μm apart). Positive current flows from Ohmic contact 1 to 6.

presented in this chapter will be published in Physical Review B [22].

6.2 Symmetric and Asymmetric Breakdown using Quantum Point Contacts

Fig. 6.2 gives a layout of sample G373B13 used in this work. Some transport parameters for this sample are listed in Table 3.1. In the figure, crosses indicate Ohmic contacts to the 2DEG; the hatched areas are split gates that are used to electrostatically define a channel of width $W_{\rm ch}$= 4 μm and length $L_{\rm ch}$= 18 μm . Two opposite pairs of quantum point contacts are defined on the top (t_1 and t_2) and bottom (b_1 and b_2) edge of the channel, with a separation of 3 μm between adjacent point contacts. The gate voltages are adjusted such that adjacent point contacts have equal resistance ($R_{t_1} = R_{t_2} \equiv R_t$ and $R_{b_1} = R_{b_2} \equiv R_b$). We present results obtained for a sample temperature of 1.65 K, and a fixed magnetic field $B = 3.45$ T, corresponding to a filling factor $\nu = n_s h/2eB = 2.0$ in the narrow channel. (Because of electrostatic depletion, n_s in the channel is somewhat smaller than in the bulk 2DEG, where $\nu = 2.08$ at 3.45 T.) A current I is passed through the channel from Ohmic contact 1 to 6. With the magnetic field direction as indicated in the figure, and for positive currents, the top edge of the channel has the highest electrochemical potential for electrons (*i.e.*, it is charged negatively). The differential resistance between Ohmic contacts i and j, $R_{ij} = {\rm d}V_{ij}/{\rm d}I$, with $V_{ij} \equiv V_i - V_j$, is measured using a low-frequency lock-in technique, see Fig. 3.2. Differential resistance data have been obtained for four different sets of values of the point contact resistances R_t and R_b. These sets correspond to different numbers (N_t, N_b) of spin-degenerate edge channels

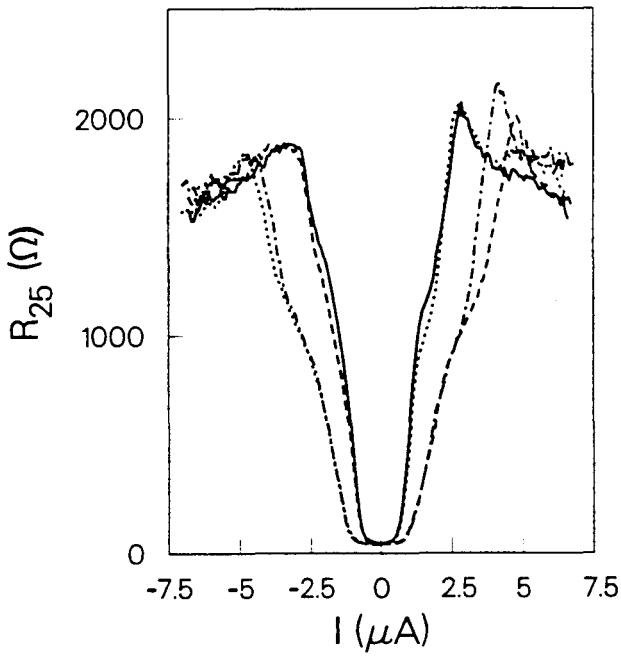

Figure 6.3: Longitudinal differential resistance R_{25} *vs.* current I for four different configurations of the point contact voltage probes: (N_t, N_b)= (2,2) (solid curve), (1,2) (dashed), (2,1) (dotted), and (1,1) (dash-dotted). (Sample G373B13).

that are fully transmitted through the point contacts on either side of the channel (note that $R_{t,b} = h/2e^2N_{t,b}$). The configurations used are (N_t, N_b)= (2,2), (1,2), (2,1), and (1,1).

In Fig. 6.3 we show the current dependence of the longitudinal differential resistance of the channel (R_{25}), measured with voltage probes adjacent to the channel. Contacts 2 and 5 are ideal voltage probes in that they equally populate all available edge channels [14]. The data in this figure reveal a pronounced influence of the adjustment of the point contacts at the channel boundaries on the observed Hall breakdown characteristics. For the set (N_t, N_b)= (2,2) (solid curve) the breakdown occurs at a relatively small current, whereas for (N_t, N_b)= (1,1) (dash-dotted) considerably larger currents are required to obtain breakdown. In both cases, R_{25} is symmetric in I, at least at relatively small current levels. In contrast, the breakdown curves for the mixed sets (N_t, N_b)= (1,2) (dashed) and (2,1) (dotted) are asymmetric. Moreover, these latter curves coincide with parts of those obtained for equal point contacts [(2,2) and (1,1)] in a specific manner. This coincidence occurs whenever the point contacts at the *high-potential edge* have been adjusted similarly (a condition which depends on the current direction). *Only the adjustment of the voltage probes on the high-potential edge influences the breakdown characteristics.* Since the onset of breakdown occurs at smaller currents when the probes transmit both edge channels, we can conclude that the breakdown is enhanced by probe-

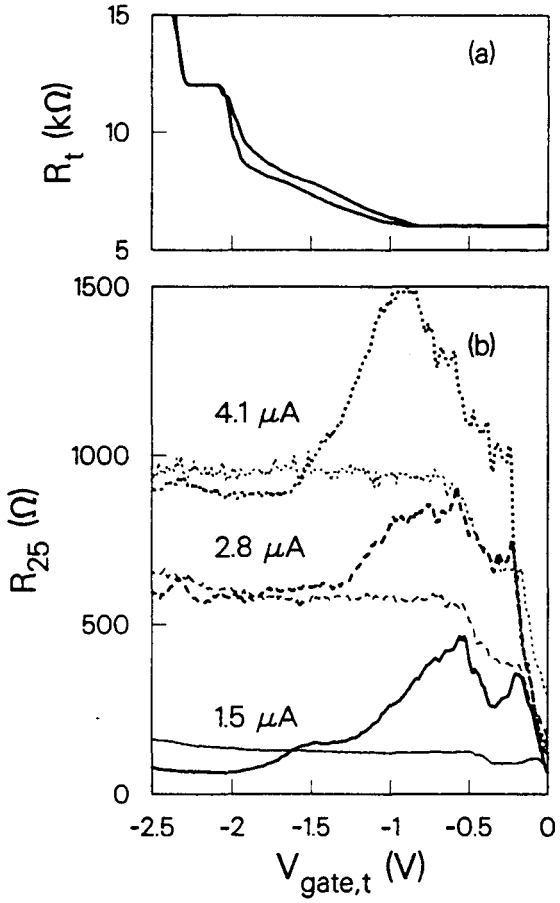

Figure 6.4: (*a*) Resistance R_t of point contacts t_1 and t_2 as a function of gate voltage. (*b*) Dependence of the longitudinal differential resistance R_{25} on the top gate voltage $V_{gate,t}$ used to define point contacts t_1 and t_2. Data are shown for three current levels, and for both current directions; thick curves refer to positive, thinner curves to negative currents. In all cases N_b= 1. (Sample G373B13).

induced *equilibration* between the higher and the lower edge channels, but only when this equilibration occurs at the high-potential edge.

More detailed information on the influence of the point contact resistance on the breakdown characteristics can be obtained from Fig. 6.4, where we show the dependence of R_{25} on the gate voltage $V_{gate,t}$ used to define point contacts t_1 and t_2, for various values of the current, and for N_b= 1. For comparison, the upper panel shows the gate-voltage dependence of the two-terminal resistance R_t of point contacts t_1 and t_2. For negative currents (thin lines in the breakdown curves), the bottom edge is at the highest electrochemical potential. The data in Fig. 6.4 show clearly that in this case the breakdown signal does not depend on the top gate voltage $V_{gate,t}$ (except for $V_{gate,t}$ between 0 V and -0.5 V, where the channel is not well defined). For positive currents, the top edge is at the highest potential, and R_{25} does depend strongly on $V_{gate,t}$. The

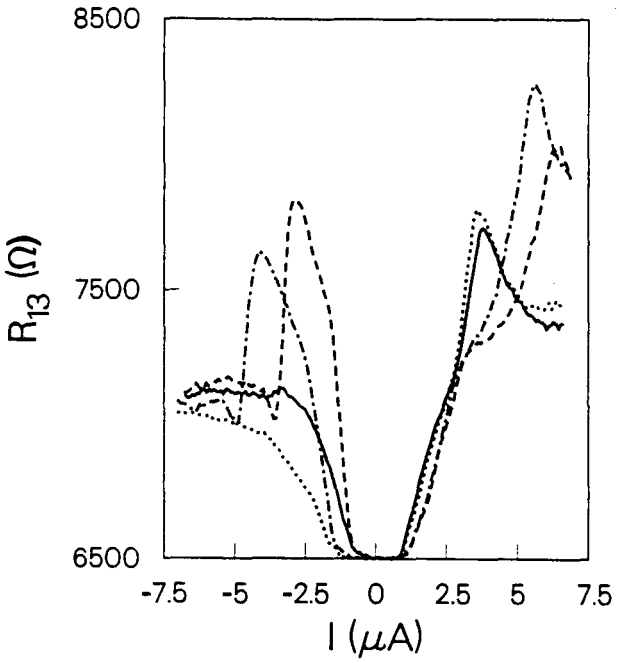

Figure 6.5: Three-terminal differential resistance R_{13} *vs.* current I for the same point contact configurations as in Fig. 6.3 (with the same coding of the curves).

breakdown is enhanced when $N_t = 2$ (corresponding to $R_t \sim 6$ kΩ). For more negative gate voltages ($N_t < 2$) the breakdown resistance R_{25} decreases, eventually reaching the value found for negative currents. These data confirm our conclusions that only the adjustment of the point contacts on the high-potential edge is of importance, and that enhanced breakdown occurs when both edge channels are transmitted through these point contacts.

Fig. 6.5 summarizes our experiments on the three-terminal differential resistance $R_{13} \equiv \mathrm{d}V_{13}/\mathrm{d}I$, measured using a quantum point contact at the top edge of the channel (3) as one voltage probe, and one of the current contacts (1) as the other. The data shown in this figure exhibit (a)symmetries similar to those in Fig. 6.3. However, in contrast to Fig. 6.3, in this case we do observe a strong effect on the breakdown data of the adjustment of the point contact at the top edge (*i.e.*, of N_t) when it is at the *lowest* electrochemical potential (negative I): when the highest occupied edge channel is not transmitted ($N_t = 1$), R_{13} is, at small negative I, much larger than for $N_t = 2$. This effect arises because contact 3 is not an ideal voltage probe, its potential being determined by the transmission of point contact t_1(*cf.* the experiments on the anomalous integer quantum Hall effect [15,16,17]). Our data imply that, under breakdown conditions, the edge channels with quantum number $n \geq 2$ at the low-potential edge are not in equilibrium with the lowest ($n = 1$) edge channel. (We write $n \geq 2$ instead of $n = 2$, because *inter*-Landau level scattering becomes energetically allowed at large Hall voltages. Our

experimental data allow the possibility of a non-equilibrium population involving also Landau levels with $n > 2$ (which are not populated in equilibrium).) This is direct evidence of *selective backscattering* in the highest occupied Landau levels, reminiscent of the selectivity causing [18,23] the Shubnikov-de Haas oscillations in the linear regime. On further increasing the negative current in the channel, the anomalously large value of R_{13} suddenly drops to the value measured for $N_{t_1} = 2$. Since the Hall voltage is too small to substantially affect the resistance of point contact t_1, our observation implies that for these current levels the edge channels at the low-potential edge equilibrate on distances short compared to the channel length. A breakdown of adiabatic transport at large current densities was also reported by Komiyama et al. [16], and was attributed to the large difference in electrochemical potential between two adjacent edge channels [24].

6.3 Interpretation: Selective Backscattering

Hall-voltage induced selective backscattering can be qualitatively understood, as follows. Fig. 6.6(a) depicts the variation of the energy of the highest Landau level along a cross section of the narrow channel at finite positive current [21]. The thick lines symbolize the occupied edge states: the solid line indicates electrons moving along the high-potential edge, and the dashed line refers to electrons moving along the low-potential edge in the opposite direction. The arrows indicate backscattering from the high-potential (t) to the low-potential (b) edge. For states at the high-potential edge with an energy E such that $\mu_b < E \leq E_0 + eV_{\rm Hall}$, where E_0 is the bottom of the Landau level, we have a situation where the overlap of the wavefunction of these occupied states and empty edge states on the low-potential edge can be continuously increased by increasing the current in the channel, and consequently the Hall voltage $V_{\rm Hall}$. This results in enhanced backscattering. Irrespective of the details of the backscattering mechanism (direct vs. impurity assisted, inter- or intra-Landau level), one can state that for lower Landau levels the current, in the same Hall voltage regime, has a much smaller influence on the overlap between occupied high-potential and empty low-potential edge states. Consequently, Hall-voltage induced backscattering occurs predominantly in the highest occupied Landau level (and, possibly, into still higher unoccupied Landau levels).

The observed effects of the adjustment of the point contacts on the breakdown can be explained by means of Fig. 6.6(b) and (c), which show the location of the edge channel wave function in the higher Landau level for $N_t = 1$ and 2, respectively (the lower Landau level has been omitted for clarity). In both situations, electrons entering the narrow channel region along the top edge in the highest Landau level are backscattered

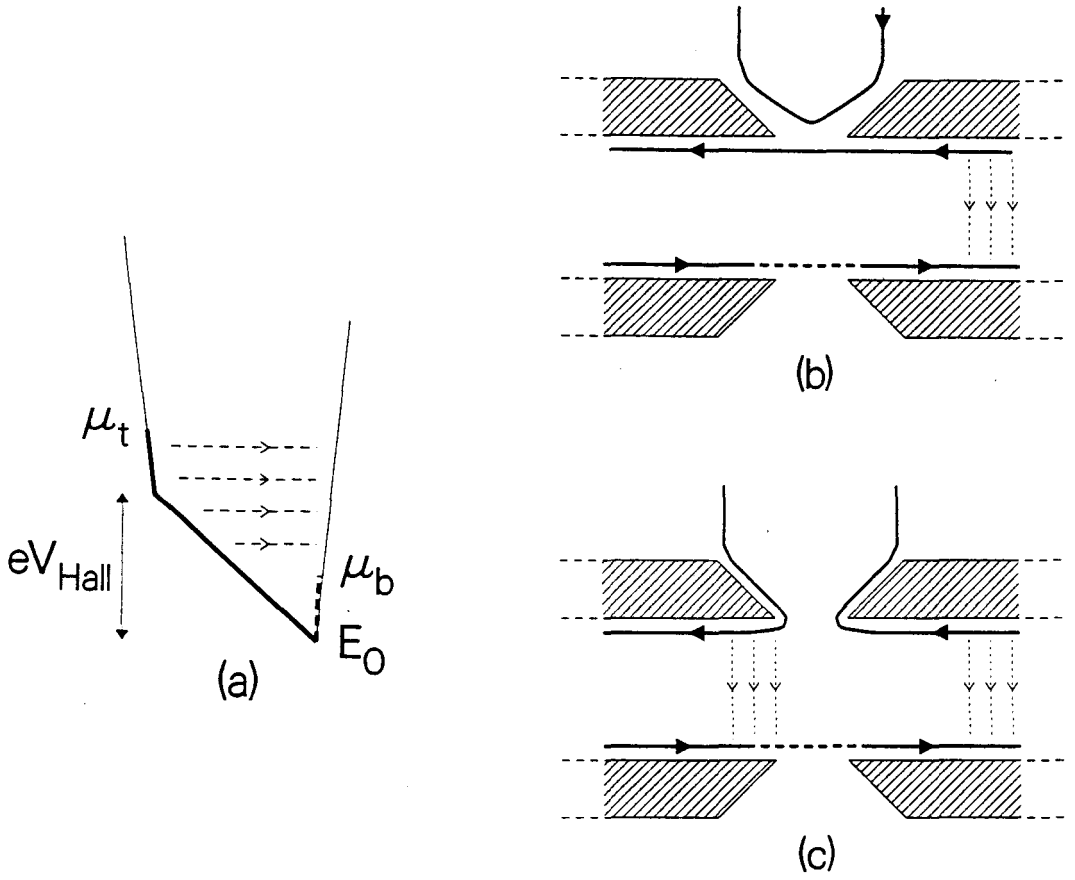

Figure 6.6: (a) Schematic energy diagram of the highest occupied Landau level along a cross section of the narrow channel. (b) and (c) Edge channels in the highest occupied Landau level. When $N_t = 1$, as in (b), backscattering occurs predominantly at the entrance of the channel, while for $N_t = 2$, as in (c), equilibration between the Landau levels in the region behind the point contact on the high-potential edge causes a second opportunity for backscattering. The transmission of the edge channel by the point contact on the potential edge (dashed) is irrelevant.

due to the proximity of the edge channel at the opposite edge. The reverse process is also possible, so that eventually a steady state situation is reached, with a partially depleted population of the higher edge channel at the high-potential edge (corresponding to a certain non-zero longitudinal resistance). This steady state is reached close to the channel entrance. If, however, the highest Landau level is transmitted by the point contact (Fig. 6.6(c), $N_t = 2$), the edge channels are equilibrated. This causes a repopulation of the partially depleted higher channel, and consequently a second opportunity for backscattering, which did not exist for $N_t = 1$.

The observed asymmetry in the breakdown curves between (N_t, N_b)= (2,1) and (1,2) is intrinsically a non-linear response effect, because it implies a dependence of the resistance on the direction of the current. We have attempted to model our observations by incorporating an energy-dependent backscattering probability in the standard Landauer-Büttiker formalism [14]. While we do find asymmetries in the breakdown curves depending on the direction of the current, our over-simplified model does not yield a satisfactory quantitative agreement with the experimental curves.

6.4 Conclusion

Breakdown of the quantum Hall effect in a narrow channel at large current densities is an unequivocal demonstration of non-linear response in the quantum Hall regime. The breakdown is accompanied by a non-equilibrium population of edge channels. As we have shown, the use of quantum point contacts is advantageous in unravelling the breakdown mechanism, since point contact voltage probes can be used for controlled equilibration and selective detection of the edge channels. Our experimental results demonstrate that breakdown of the quantum Hall effect proceeds predominantly via *selective* backscattering within the highest Landau levels. This is qualitatively understood by the increasing overlap of wave functions of occupied high-potential and empty low-potential edge states with increasing Hall voltage.

Further studies using quantum point contacts could reveal the details of the backscattering mechanism. For instance, experiments at non-integer values of the filling factor ν may discriminate between inter- or intra-Landau level backscattering. It must be noted that ν is also sensitive to the gate voltages used to define the 4 μm wide channel. Thus either the magnetic field must be adapted for different settings of the point contacts to yield the same value for ν in such an experiment, or a wider channel must be used. Symmetries and asymmetries could also be studied for different adjustments of adjacent point contacts, $(N_{t_1}, N_{t_2}) = (N_{b_1}, N_{b_2}) = (1,1),\ (1,2),\ (2,1),\ (2,2)$. In combination with experiments on channels with different lengths, different geometries of

entrance and exit, and different separation distances between the point contacts, these experiments should yield information about the dependence of the breakdown on length and geometry of the constrictions.

Chapter 7

Electron–Electron Interactions in the Ballistic Regime

7.1 Introduction

The ability to create a collimated electron beam in a 2DEG using a point contact as an electron injector, as described in Section 2.3, allows for the study of crossing electron beams reminiscent to crossing beam experiments in vacuum. Such an experiment would directly reveal information of ballistic electron interactions, which are up to now only studied via dephasing experiments [25]. In contrast to two isolated electrons in vacuum, which interact via the long range $\sim r^{-1}$ Coulomb potential, the degenerate 2D electron gas effectively screens the Coulomb interaction due to the high electron density. So the repulsion between the ballistic electrons in a 2DEG is strongly reduced due to the highly polarizable background. From the Thomas-Fermi screening wave vector for 2D, given by

$$q_{\mathrm{TF}} = \frac{2}{a_{\mathrm{B}}} = \frac{me^2}{2\pi\varepsilon_{\mathrm{r}}\varepsilon_0\hbar^2} \tag{7.1}$$

where a_{B} is the effective Bohr-radius, a screening length $l_{\mathrm{TF}} = 1/q_{\mathrm{TF}}$ can be calculated.

To study the interaction of crossing ballistic electron beams, we designed a sample in which two perpendicular ballistic electron beams can be generated by means of point contacts. The layout is given in the inset in Fig. 7.1. A 100 μV RMS low frequency ac excitation voltage between injector i and grounded drain d produces a collimated ballistic electron beam which is detected as a non-local voltage by the collector c. The injector–collector distance is 3.3 μm. The three terminal zero-field collimation signal $V_{\mathrm{c}}/I_{\mathrm{i}}$ is monitored as function of a negative dc current from m to d, which results in a dc ballistic collimated beam that intersects the ac beam. The distance between modulating point contact m and the crossing point is 1.3 μm, and the injector – crossing point distance is 2.0 μm. Negative gate voltages were applied to the gates, and adjusted

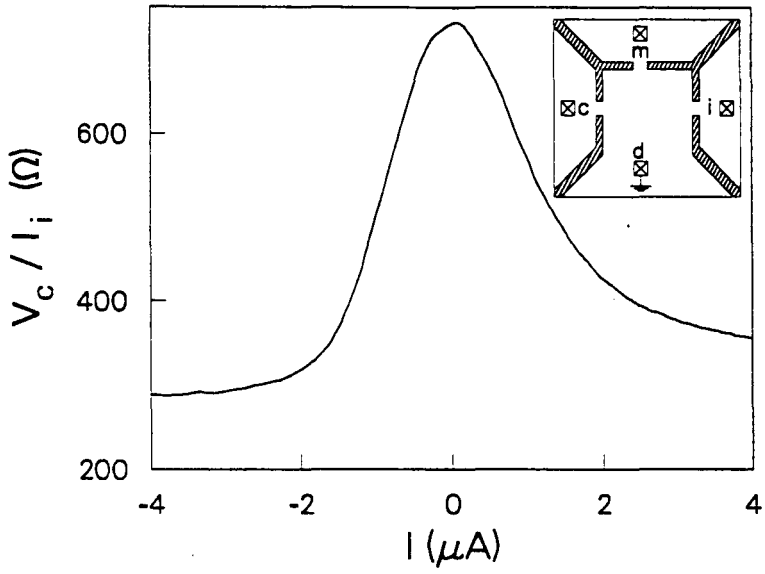

Figure 7.1: Collimation signal for zero magnetic field, using injector i and detector c as shown in the inset, as function of a dc current through point contact m. In the sample layout given in the inset gates are indicated as hatched areas and the crosses refer to Ohmic contacts to the 2DEG. Ohmic contact d is used to drain the by i and m injected electrons and is also used as a voltage reference for the collector c. (Sample G627D19).

such that in all three point contacts three 1D subbands were occupied ($N = 3$).

In Fig. 7.1 a typical result of V_c/I_i as a function of I_{dc} is shown, obtained from sample G627D19. Increasing the negative dc current from $I = 0$ μA to $I = -2$ μA dramatically reduces the ac collimation signal from 720 Ω to about 300 Ω, while increasing the dc current beyond -2 μA does not further affect the signal significantly. A similar behavior is observed for positive current, where a slightly weaker and more gradual dependence on the current is observed. It must be noted that the measurement configuration in Fig. 7.1 is three-terminal, so that V_c/I_i includes the resistance of the Ohmic contact m, which is ~ 300 Ω. Thus we see that, after correction for the Ohmic contact resistance, the dc collimated electron beam (generated by a negative dc current) completely destroys the ac collimation signal.

Let us try to interpret this ballistic electron beam interaction in terms of direct ballistic electron collisions, by comparing the inter-electron distances in the collimated beams to the Thomas-Fermi screening length, see Eq.(7.1). In the presence of collimation, the current transverse to a line segment $dw = rd\phi$ at a distance r from a point contact can, using Eq.(2.8), be written as

$$dI = \frac{If\cos\phi}{2r} dw \times e^{-r/l_e} \tag{7.2}$$

From the current density $j = \mathrm{d}I/\mathrm{d}w = nev$ and the semi-classical expression for the collimation factor, Eq.(2.10), the ballistic electron density at the center of the beam ($\phi = 0$) is derived

$$n_{ball}(r, \phi = 0) = \frac{Ik_{\mathrm{F}}W_{\max}}{2\pi eNvr} \times e^{-r/l_{\mathrm{e}}} \tag{7.3}$$

For the dc collimated beam we estimate the electron velocity v simply from $\frac{1}{2}mv^2 = E_{\mathrm{F}} + e|V|$, which gives $v^{\mathrm{dc}} = \sqrt{(2eNE_{\mathrm{F}} + h|I|)/eNm}$, whereas for the electrons in the ac beam we assume $v^{\mathrm{ac}} = v_{\mathrm{F}}$. Using the sample parameters as listed in Table 3.1 for sample G627D19 and assuming that $W_{\max}$ equals the lithographic opening of the point contacts of 200 nm (which is not unreasonable to do, see Ref.[7]), we calculate the ballistic electron density n_{ball} and the distance between ballistic electrons $l_{\mathrm{ball}} = 1/\sqrt{\pi n_{\mathrm{ball}}}$ in the two collimated beams at the crossing point. For a dc current of -2 μA, for which the ac signal is almost disappeared, this calculation yields $n^{\mathrm{dc}}_{\mathrm{ball}} = 4.3 \times 10^9$ cm^{-2} and $l^{\mathrm{dc}}_{\mathrm{ball}} = 86$ nm, and for the 100 μV ac signal $n^{\mathrm{ac}}_{\mathrm{ball}} = 4.2 \times 10^7$ cm^{-2} and $l^{\mathrm{ac}}_{\mathrm{ball}} = 0.87$ μm is obtained. The screening length $1/q_{\mathrm{TF}}$, calculated for GaAs with effective electron mass $m = 0.067 \times m_{\mathrm{e}}$ (m_{e} is the free electron mass) and $\varepsilon_{\mathrm{r}} = 13.1$, is $l_{\mathrm{TF}} = 5.2$ nm. This is very small compared to $l^{\mathrm{dc}}_{\mathrm{ball}} = 86$ nm at $I = -2$ μA, thus we can not contribute the experimental result of in Fig. 7.1 to ballistic electron–ballistic electron collisions.

The arguments given above only lead to a crude estimate for both inter-electron distance in a collimated beam and screening length. We have, *e.g.*, used the semi-classical relation between collimation factor and point contact resistance, whereas in the experiment the point contact resistances were set to the quantized $N = 3$ plateau-value. Furthermore, the Thomas-Fermi screening length is independent of electron density, which only holds for the highly-degenerated case (high densities). However, as also is indicated by the decrease in collimation signal for positive currents, it is not plausible that the result of Fig. 7.1 can be explained in terms of ballistic electron–ballistic electron collisions, even when accounting for the above. A similar conclusion may be drawn from the result of Spector *et al.*[26] that two ballistic electron beams show negligible mutual interaction upon penetrating each other. In that experiment two low amplitude (1 μA RMS) low frequency ac ballistic electron beams cross perpendicular halfway between injector and collector. To determine the cross-talk between the two ballistic beams two different ac excitation frequencies were used and detection was performed at both frequencies. Switching on the second beam resulted in no observable effect in the detection signal of the first beam, while no significant signal was detected at the frequency of the second beam. This implies the absence of cross-talk between the two beams. Nevertheless, Fig. 7.1 really shows a large and robust effect of the dc beam on the ac collimation signal.

7.2 Collimation as function of Electron Temperature

In the experiment of Spector *et al.*[26] a much larger injector–detector distance (26 μm) than in our experiment was used, combined with extra collimating electrodes in the region in between injector and detector. Fig. 7.1 clearly shows a non-linear effect, which is not observed in the linear response regime of Ref.[26]. As discussed in Section 2.4 (see also Ref.[5]), hot electrons injected through a point contact distribute their excess energy in the nearby 2DEG region. The decrease of the collimation signal might be a consequence of heating of the 2DEG region between injector and collector. The slightly asymmetric shape of the curve in Fig. 7.1 also might indicate a heating mechanism, because heat is mainly dissipated at the point contact side where the (hot) electrons are injected (although the Sharvin resistance of the point contact must not be neglected in heat dissipation by electrons around a point contact).

To study the influence of electron temperature we have used a 18 μm long and 4 μm wide channel with on both sides two point contacts which are 3 μm apart, see Fig. 7.2. (A similar sample was used in Chapter 6 for studying the breakdown of the quantum Hall effect.) The results presented below were obtained from sample G620D54, for which some transport parameters are listed in Table 3.1. For all collimation experiments a low frequency low amplitude excitation signal was injected through point contact i and drained to ground by contact 3. The collimation signal was obtained by measuring the ac voltage of contact 6 relative to contact 7, using the double lock-in technique (Fig. 3.2). Note that the collimation signal obtained in this configuration, $V_c/I_i = R_{13,67}$, is a four-terminal resistance that does not include any Ohmic contact contribution. The electron temperature in the channel region between the injector and collector was varied in three different ways: (i) by passing a negative dc current through the channel from contact 8 to 3, (ii) by varying the sample temperature, (iii) by injecting a negative dc current through point contact m, which is then also drained to ground by contact 3. The gate voltages were adjusted such that the resistances of both injecting and collimating point contact were $\sim h/2e^2$, which corresponds to one occupied 1D subband ($N_i \approx N_c \approx 1$). When used as modulator for the dc current, point contact m was set to $N_m \approx 4$ or $N_m \approx 1$.

In Fig. 7.3 some typical magnetic field scans of the collimation signal V_c/I_i (see also Section 2.3 and Ref.[7]) are shown for three different dc currents through the channel at $T = 1.7$ K (left panel), and for three different sample temperatures without a dc current (right panel). (A 3D representation of the complete magnetic field dependent collimation *vs.* channel–current experiment is found at the cover of this report.) The collimation

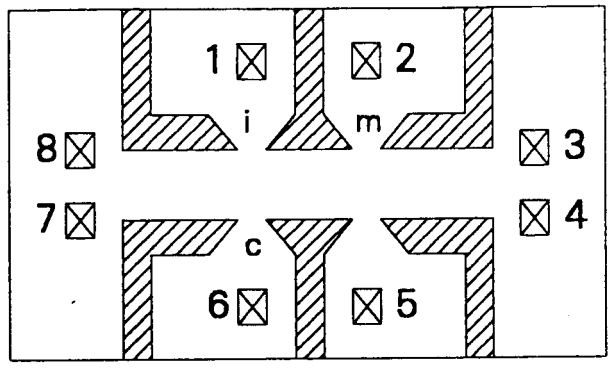

Figure 7.2: Lay out for sample G620D54. The channel defined by the gates (hatched areas) in the 2DEG is 18 μm long and 4 μm wide. Point contacts on both sides of the channel are 3 μm apart. The crosses refer to Ohmic contacts to the 2DEG. In all experiments contact 3 is grounded. The magnetic field (when used) is directed downwards.

signal disappears for either larger currents or higher temperatures. Similar curves were obtained for dc currents flowing between contacts 2 and 3, *i.e.* passing through point contact m (not shown here). The central peak at $B = 0$ T is the normal collimation peak for electrons directly travelling electrons from injector to collector. The two upper curves in Fig. 7.3 correspond to the same current and temperature ($I = 0$ μA, $T = 1.7$ K), but were obtained on two different cool-downs. In between the channel–current dependent collimation experiment (left panel) and temperature dependent collimation experiment (right panel), the sample temperature was (overnight) raised up to about 40 K. The smaller collimation signal and the less well resolved side peaks of the second $I = 0$ μA, $T = 1.7$ K experiment (upper right curve), is probably due to a slightly different frozen in impurity configuration and possibly slightly different point contact resistances.

For only one 1D subband occupied in the injecting point contact i, the point contact width equals half the Fermi wavelength and the point contact acts as a single mode point source for the injection of electrons. We interpret the side peaks, which are best resolved in the upper left trace of Fig. 7.3, a an impurity diffraction pattern, caused by electrons reaching the collector after being elastically scattered by an impurity (see also Section 4.2). This interpretation is confirmed by the observation that the diffraction pattern is well reproducible during one cool-down, but differs slightly from the pattern obtained from another cool-down.

The negative plateau value of V_c/I_i for $|B| > 20$ mT for the channel–current collimation experiment, which was also observed for the experiments where the current was injected through point contact m, is interpreted as a small longitudinal voltage drop in the channel (negative because of opposite directions of V_c and I_i). However, the slowly

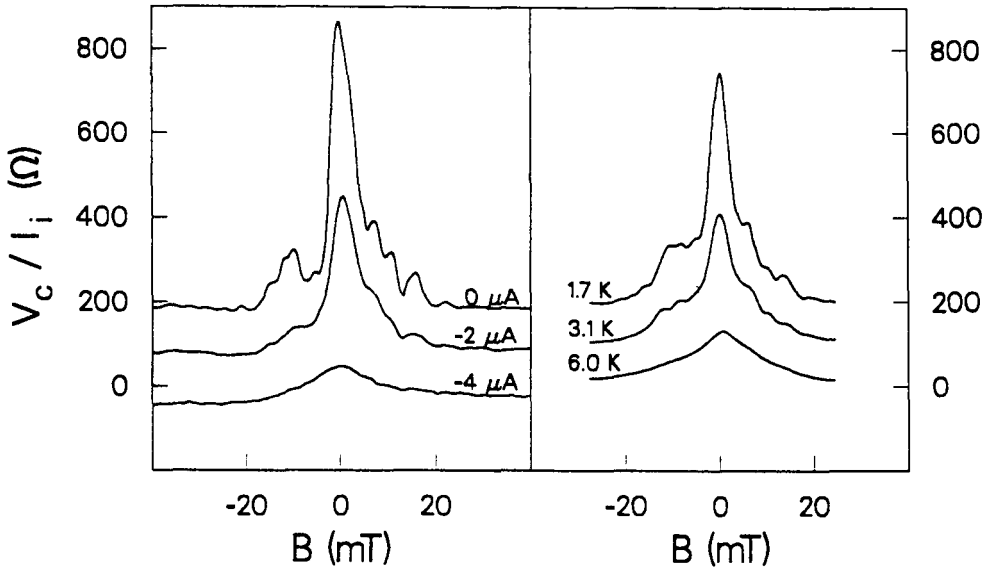

Figure 7.3: Collimation signal $V_c/I_i = R_{13,67}$ *vs.* magnetic field for different dc currents through the channel (from contact 8 to contact 3) at a sample temperature $T = 1.7$ K, left panel, and for different sample temperatures (in the absence of a dc current), right panel. For clarity, subsequent curves from bottom to top are offset by 100 Ω, with the lowest curves shown at their actual values. (Sample G620D54).

increasing *positive* plateau value with increasing sample temperature is not understood.

For a comparison of the different collimation experiments we define a normalized collimation signal R/R_0 which is the zero-field peak height $[V_c/I_i]^{\text{peak}}$, measured relative to the plateau value at $B = -0.25$ mT, for a given current or temperature, normalized to the peak height for zero current and $T = 1.7$ K

$$\frac{R}{R_0} = \left[\frac{V_c}{I_i}(T, I)\right]^{\text{peak}} \Big/ \left[\frac{V_c}{I_i}(T = 1.7 \text{ K}, I = 0\ \mu\text{A})\right]^{\text{peak}} \tag{7.4}$$

This normalized collimation peak value R/R_0 is measured as a function of a channel-current, sample temperature and current injected through modulation point contact m. The results are shown in Fig. 7.4. In all three cases, the collimation signal is affected in a similar way. The results show that ballistic electron – ballistic electron scattering is not the mechanism for the decrease in collimation signal. In the experiment where the dc current is injected through point contact m the hot ballistic electrons do not reach the region between injector and collector. In all experiments shown in Fig. 7.4 somehow the electron temperature in the region in between injector and collector is raised: for (*a*) the current in the channel dissipates Joule heat in the channel, in (*b*) the electron temperature equals the increasing sample temperature, and in (*c*) heat dissipated at

point contact m is distributed by heat conduction in the 2DEG (see Section 2.4 and Ref.[5]). Thus the experiments suggest that the mean free path for ballistic electrons, which is directly probed by the collimation experiment, decreases with increasing electron temperature in the 2DEG. A possible mechanism for this will be proposed in the next section.

7.3 Quasiparticle Lifetime in a Fermi Liquid

The usual model for the sheet of conducting electrons at the heterostucture interface, which we have used so far, is a *non-interacting* two dimensional electron gas with the electrons obeying Fermi-Dirac statistics. This model holds in the linear response regime at low temperatures due to not only the screening of the long range Coulomb potential in a degenerate electron system, as discussed in the previous section, but also because of the Pauli exclusion principle. Consider, *e.g.* a 2DEG in thermal equilibrium at $T = 0$ K, for which all the electron states within the Fermi circle are filled and all the states with $E > E_F$ are empty. According to the Pauli exclusion principle, a two-electron collision in this 2DEG is only allowed when the electrons scatter into empty states. Energy conservation demands that the sum of energies of the initial states, which is $\leq 2E_F$ because only states within the Fermi circle are initially occupied, equals the sum of the final state energies. However, because all empty states lie outside the Fermi circle, the Pauli principle prohibits electron scattering in this system [27].

For an electron system where states E_1^i and E_2^i are occupied and states E_1^f and E_2^f are empty and for which $E_1^i + E_2^i = E_1^f + E_2^f$ is satisfied, electrons in the initial states E^i are allowed to scatter into the final states E^f. The model of a non-interacting electron gas fails to describe this electron system, but Fermi-liquid theory provides a model that accounts for electron-electron interactions in a 2DEG (see Ref.[28] for the theory of charged Fermi liquids). The Fermi liquid theory is based on the concept of interacting *quasiparticles* obeying Fermi-Dirac statistics. A quasiparticle is an elementary excitation in the Fermi liquid, *e.g.* an excitation outside the sharp defined Fermi surface at $T = 0$ K, in close analogy with a single-particle excitation of a non-interacting Fermi gas. So in an interacting 2DEG a quasiparticle is obtained if an electron occupies an otherwise empty state above the Fermi level (assume $T = 0$ K). Due to the mutual (screened) Coulomb interaction, the quasiparticle state is not stationary, and redistribution of energy and momentum among the electrons causes a quasiparticle state to decay. This leads to a finite inelastic lifetime τ_{e-e} for the quasiparticles. Quasiparticles can decay via two elementary mechanisms: (i) via single electron-hole pair excitations and (ii) via excitation of plasma modes. We only take the first process

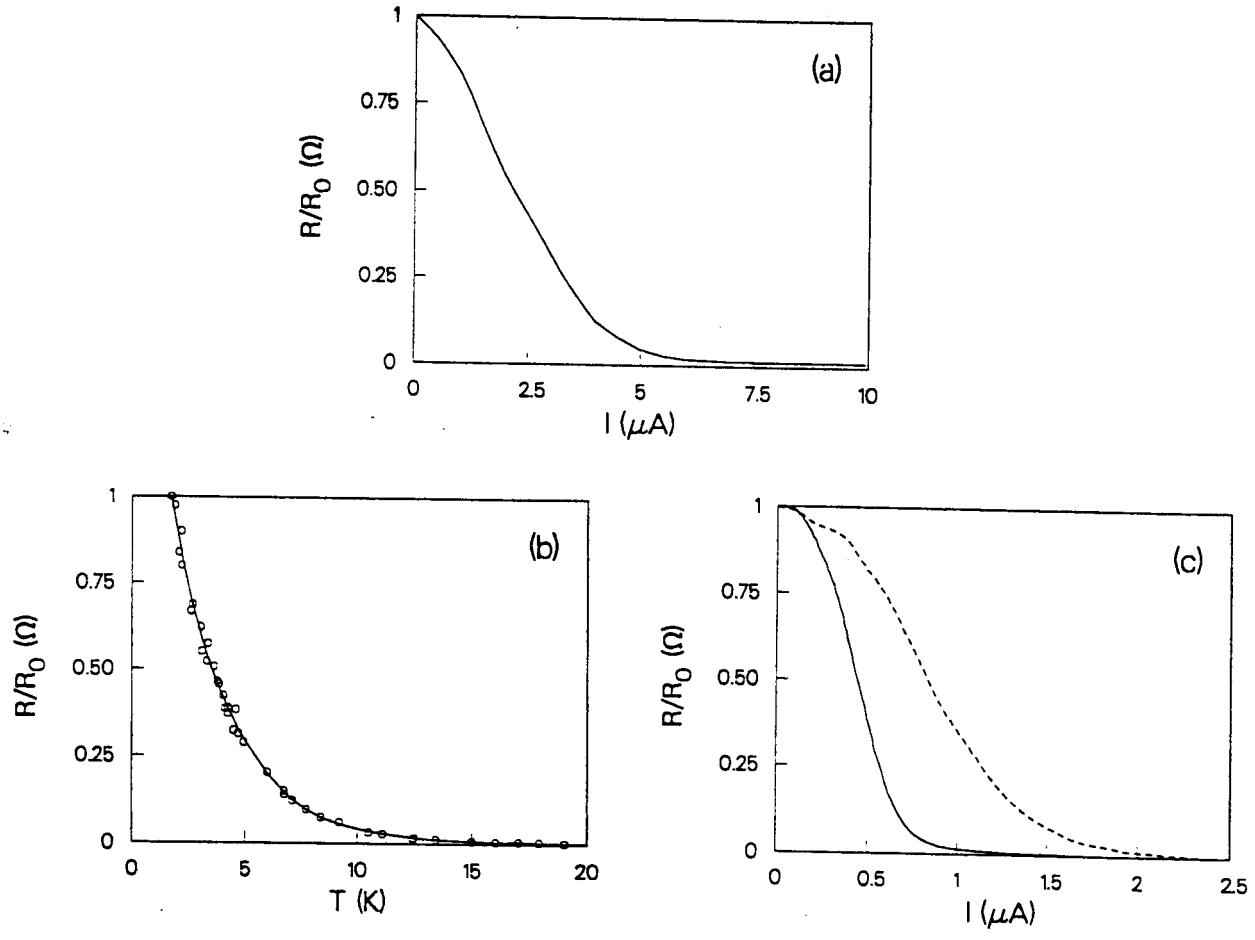

Figure 7.4: Normalized collimation peak value R/R_0 defined by Eq.(7.4) as function of (a) a dc current through the channel at sample temperature $T = 1.7$ K, (b) sample temperature in the absence of a dc current, and (c) a dc current through point contact m for $T = 1.7$ K , with $N_m \approx 4$ (dashed) and $N_m \approx 1$ (solid). The data as function of temperature in (b) are obtained from magnetic field scans at different temperatures, as shown in Fig. 7.3. The solid line in (b) is a guide to the eye. (Sample G620D54).

into account, because we estimate from Fig. 3 of Ref.[29] for a 2DEG with electron density $n_s = 2 \times 10^{11}$ cm^{-2} (which approximates n_s of sample G620D54, see Table 3.1) a threshold energy for plasmon emission of $E_{pl} \approx 3.2E_F$, which is much larger than the quasiparticle energies achieved in our experiments.

The quasiparticle lifetime due to single electron-hole pair excitations for a 2DEG was calculated by Giuliani and Quinn [30] for an electron system at $T = 0$ K as function of the quasiparticle excitation energy Δ relative to the Fermi energy as

$$\frac{1}{\tau_{e-e}} = \frac{E_F}{2h}\left(\frac{\Delta}{E_F}\right)^2\left[\ln\left(\frac{E_F}{\Delta}\right) + \ln\left(\frac{2q_{TF}}{k_F}\right) + \frac{1}{2}\right],\ T = 0\text{ K},\ \Delta \ll \frac{\hbar^2 k_F q_{TF}}{m} \qquad (7.5)$$

and for an electron system with negligible excitations as function of the 2DEG temperature as

$$\frac{1}{\tau_{e-e}} = \frac{E_F}{h}\left(\frac{k_B T}{E_F}\right)^2\left[\ln\left(\frac{E_F}{k_B T}\right) + \ln\left(\frac{2q_{TF}}{k_F}\right) + 1\right],\ \Delta \ll k_B T \ll E_F \qquad (7.6)$$

where q_{TF} is the 2D Thomas-Fermi screening wave vector given by Eq.(7.1). Thus according to the Fermi-liquid theory electron–electron scattering increases with increasing electron temperature, due to the increase in phase space available for this process because of thermal smearing of the Fermi-Dirac distribution. Assuming $v = v_F$ for the electron velocity, we can calculate a temperature dependent mean free path for electron–electron scattering $l_{e-e} = v_F \tau_{e-e}$ from Eq.(7.6), using the transport parameters as listed in Table 3.1 for sample G620D54. The result of this calculation is shown in Fig. 7.5, and it is seen that l_{e-e} equals the injector–collector distance of 4 μm of sample G620D54 for $T = 6.9$ K.

Assuming a Lambert–Beer like exponential behavior for the electrons detected by the collector c, we can now simply compare the temperature dependent zero-field collimation signal from Fig. 7.4(b) to an exponential function $\exp(-L/l_{e-e})$, where L is the distance between injector and collector. Because R/R_0 is normalized to unity for $T = 1.7$ K (see Eq.(7.4)), R/R_0 must be multiplied in such a comparison by 0.924, which is the value of $\exp(-L/l_{e-e})$ for $T = 1.7$ K. As shown in Fig. 7.6 the exponential decay, derived from the quasiparticle lifetime expression Eq.(7.6), is of the same order of magnitude as the temperature dependent behavior of the collimation signal. However, the collimation signal decreases faster with temperature than predicted by the Fermi liquid theory. This indicates that, besides electron–electron collisions, additional scattering processes reduce the collimation signal with increasing temperatures. In the experiment of Fig. 7.6 the collimation signal was measured as function of the sample temperature, thus not only the electron temperature was increased, but the lattice was also heated. Therefore, maybe the deviation between theory and experiment in Fig. 7.6 can partly be attributed to additional acoustical phonon scattering. The temperature

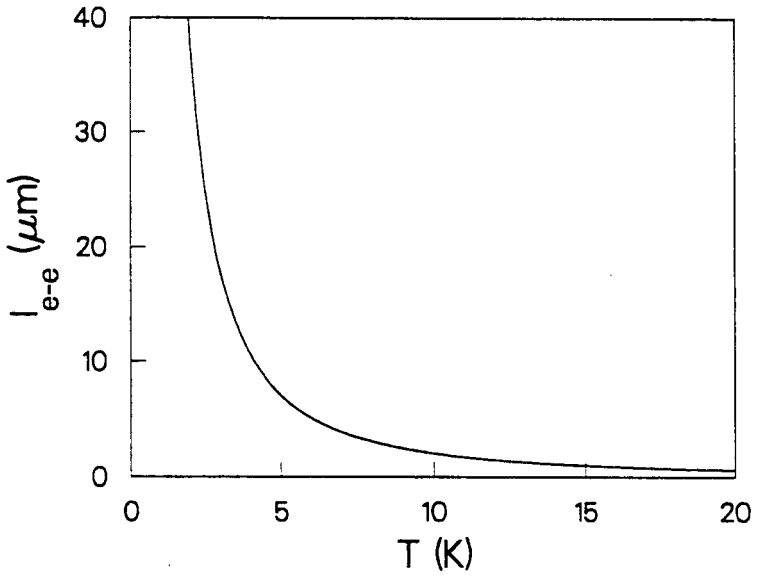

Figure 7.5: Electron–electron mean free path *vs.* electron temperature, calculated from the temperature dependent quasiparticle lifetime $\tau_{e-e}(T)$ given by Eq.(7.6), using $l_{e-e} = v_F \tau_{e-e}$ and the transport parameters as listed in Table 3.1 for sample G620D54.

dependent electron–phonon scattering rate according to Leadly *et al.*[10] is an order of magnitude too small to lift the complete discrepancy. However, this value is based on inelastic electron–phonon scattering, whereas our experiment is also sensitive to elastic electron–phonon scattering. The elastic electron–phonon scattering rate is not known, but certainly larger than the inelastic scattering rate.

In addition to this, the point contact conductance shows an anomalous dependence on the temperature [31]: G increases with increasing sample temperature until a maximum is reached at $T \sim 10 - 20$ K, beyond which G starts to decrease. Thermal ionization of shallow donors yielding a changing capacitance between gates and 2DEG may play a role [31], but the exact mechanism is not yet understood. The collimation signal is given by

$$\frac{V_c}{I_i} = \frac{2e^2}{h} \frac{T_{i \to c}}{G_i G_c} \tag{7.7}$$

where $T_{i \to c}$ is the transmission from injector to collector and G_i and G_c are the conductances of injector and collector respectively. Thus the temperature dependence of the point contact conductance may also partly be responsible for the discrepancy in Fig. 7.6.

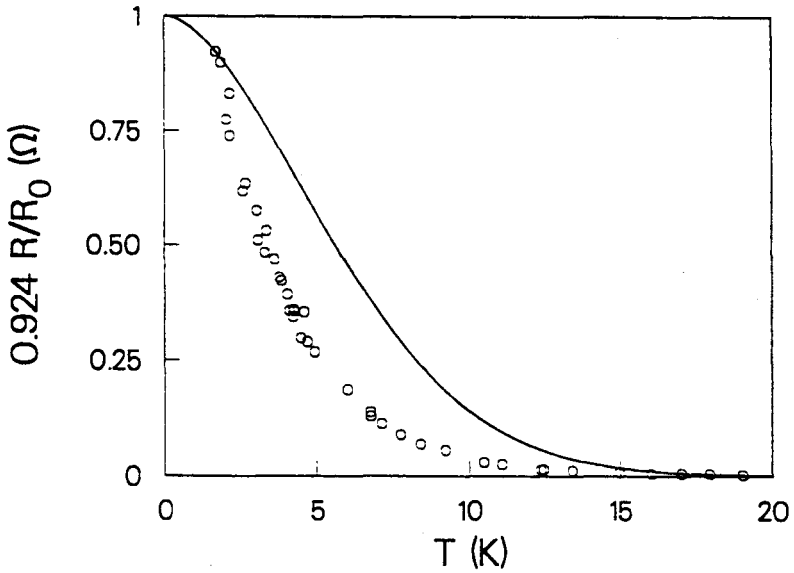

Figure 7.6: Comparison of the temperature dependent collimation signal (see Fig. 7.4) (circles) with $\exp(-L/l_{e-e})$ with l_{e-e} the electron-electron mean free path calculated from the quasiparticle lifetime (solid line). The collimation signal R/R_0 is multiplied by 0.924, which is the value of $\exp(-L/l_{e-e})$ for $T = 1.7$ K to account for the normalization of R/R_0 to the experiment at $T = 1.7$ K. (Sample G620D54).

7.4 Electron Heating by a dc Current

We assume that in the experiments where the collimation signal is monitored as function of a dc current only, the electron gas is heated, while the lattice remains at temperature $T = T_0 = 1.7$ K. Comparing the (inelastic) electron–phonon relaxation time at $T_0 = 1.7$ K, $\tau_{e-p} \approx 2$ ns [10], with the electron–electron relaxation time at electron temperature $T_e = 5.0$ K, $\tau_{e-e} \approx 35$ ps (see Eq.(7.6)), indeed confirms the possibility of a thermalized electron sea at T_e in a lattice with uniform temperature $T_0 < T_e$. Although the current dependent collimation experiments do not suffer from problems concerning high lattice temperatures, determination of the electron temperature for a given current is the main problem in the comparison of these experiments with Fermi liquid theory.

As discussed in Section 2.4, the thermopower of a point contact can in principle be used to determine the temperature difference between two 2DEG regions separated by the point contact [5]. We have used this mechanism to measure the electron temperature in the 2DEG region in between injector and collector in the following way. For a small dc current through the channel (-3 μA from contact 8 to contact 3) we have monitored the oscillating transverse dc voltage $V_1 - V_6$ as function of the gate voltage of point contact c. Point contact i was just defined by a small (~ -0.4 V) gate voltage, so

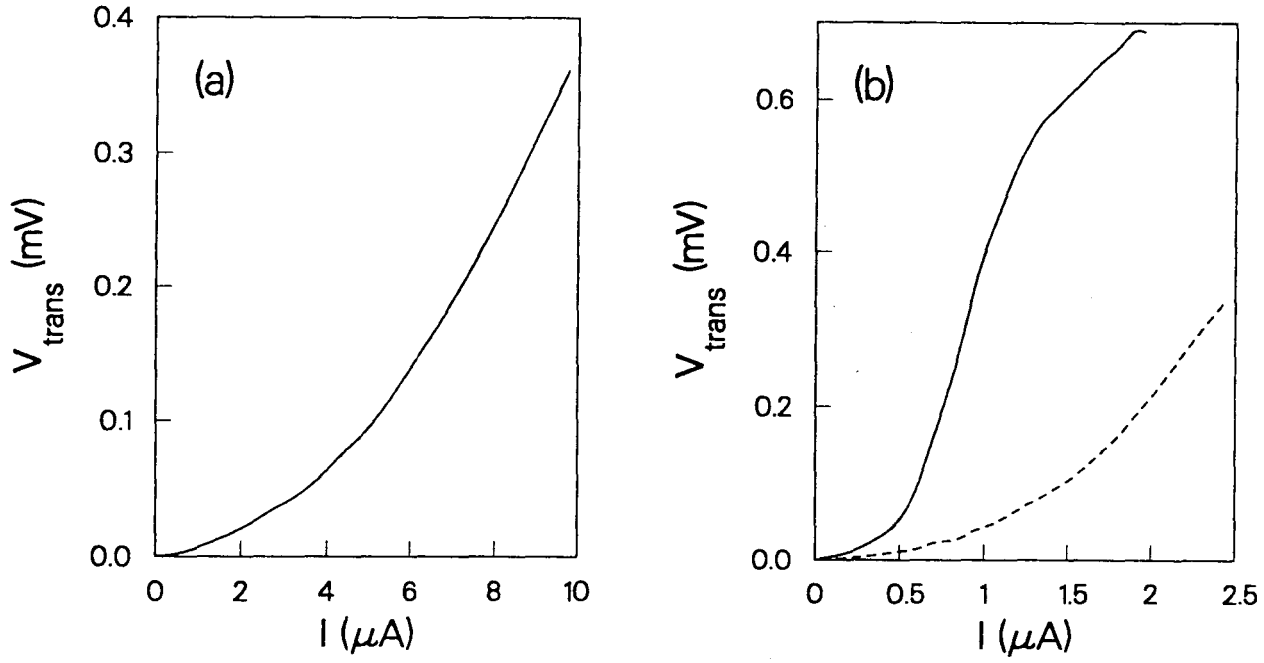

Figure 7.7: Transverse dc thermovoltage $V_{\text{thermo}} = V_1 - V_6$ *vs.* a dc current through (a) the channel, from contact 8 to contact 3, and (b) through point contact m (from contact 2 to contact 3) at $T = 1.7$ K. The gate voltages were such that point contact i was just defined and ($N = \frac{1}{2}$) for point contact c, corresponding to a maximum in the thermovoltage of c. Point contact m in (b) is adjusted such that $N = 1$ (solid line) or $N = 4$ (dashed). (Sample G620D54).

that no thermovoltage could develop across this reference point contact. Point contact c was adjusted such that the thermovoltage $V_{\text{thermo}} = V_1 - V_6$ was at a maximum, between the $N = 1$ and $N = 2$ plateaus. For these fixed gate voltages V_{thermo} was then measured as function of (i) a negative dc current through the channel, Fig. 7.7(a), and (ii) a negative dc current through point contact m with four and one 1D subbands occupied respectively, see Fig. 7.7(b). As expected for Joule heating, V_{thermo} is in good approximation quadratic in the current, except for the current through m with $N = 1$. This may partly be due to the non-linear $I - V$ characteristic for this high resistance point contact.

We should now be able to derive the electron temperature T_e as function of the current, combining the experiments of Fig. 7.7 with Eq.(2.18) (with $N = 1$). However, Eq.(2.18) leads to an overestimate of the electron temperature due to the assumption of an ideal step function for the transmission of the quantum poin contact. For a quantum point contact electrostatically defined in a 2DEG with a pair of split gates, the potential of the constriction is a smooth function, which can conveniently be modeled by a saddle potential (see Fig. 2.1). This was recently demonstrated by Büttiker [32], who used the

potential

$$V(x,y) = V_0 - \frac{1}{2} m \omega_x^2 x^2 + \frac{1}{2} m \omega_y^2 y^2 \tag{7.8}$$

where V_0 is the electrostatic potential at the saddle and the curvatures of the potential are expressed in terms of frequencies ω_x and ω_y (the y-direction is transverse to the point contact axis). This potential yields a transmission of incident channel n to outgoing channel m of [32]

$$T_{mn} = \delta_{mn} \frac{1}{1 + e^{-\pi \varepsilon_n}} \tag{7.9}$$

with

$$\varepsilon_n = \frac{2[E - \hbar\omega_y(n + \frac{1}{2}) - V_0]}{\hbar\omega_x} \tag{7.10}$$

This transmission function can now be inserted in Eq.(2.17), and by taking a realistic value of ω_x/ω_y, obtained from fitting experimental gatescans to Eq.(7.9), V_{thermo} can be calculated as function of temperature. However, we will follow another procedure.

Assume that V_{thermo} as shown in Fig. 7.7 is in first order a linear function of the temperature difference between heated channel region with electron temperature T_e and cold 2DEG regions at lattice temperature T_0 behind the point contacts

$$T_e = cV_{\text{thermo}} + T_0 \tag{7.11}$$

Parameter c [K/V] can then be used as fitting parameter in the comparison of the channel–current dependent collimation signal (Fig. 7.4(a)) and the Fermi liquid theory prediction $\exp(-L/v_F\tau_{e-e})$ with τ_{e-e} given by Eq.(7.6). The quasiparticle lifetime τ_{e-e} as function of the current is calculated using Eq.(7.11) and the experimental V_{thermo} as function of the current. A reasonable agreement between experiment and theory is obtained for $c = 1.7 \times 10^5$ K/V, as shown in Fig. 7.8. This fitted value of c is a factor 10 larger than $e/k_B \ln(2) = 1.67 \times 10^4$ K/V that follows from Eq.(2.18).

The three current dependent collimation peak signals, Fig. 7.4, can be compared directly by plotting R/R_0 *vs.* V_{thermo}, see Fig. 7.9. Provided that in all experiments the current yields the same distribution of electrons between injector and collector, R/R_0 should show the same dependence on V_{thermo} for the three cases. However, as shown in Fig. 7.9, for I through m with $N = 1$, R/R_0 shows the weakest dependence on V_{thermo}, and for I through the channel, R/R_0 shows the strongest dependence on V_{thermo}. This indicates that for current injection through point contact m the injected hot electrons are not yet completely thermalized when they reach the region between i and c. Apparently, the larger the deviation from a thermalized Fermi-Dirac distribution, the larger thermovoltage is obtained for the same value of R/R_0.

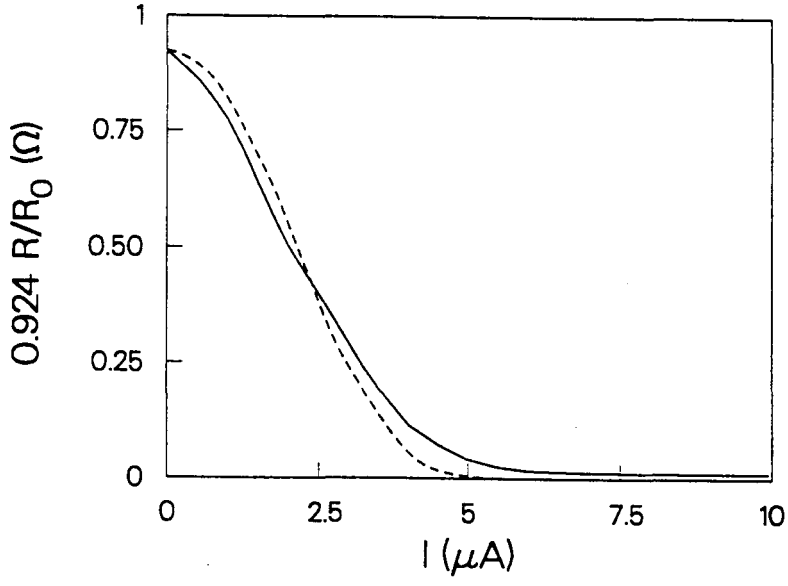

Figure 7.8: Normalized collimation peak signal 0.942 R/R_0 (solid line) and Fermi liquid theory prediction $\exp(-L/v_F\tau_{e-e})$ with $L = 4$ μm (dashed) as function of a dc current through the channel. The quasiparticle lifetime τ_{e-e} as function of the current is derived from a thermovoltage measurement, as described in the text. The fitted value of c of Eq.(7.11) is 1.7×10^5 K/V. (Sample G620D54).

7.5 Conclusion

We have shown that, although the high ballistic electron densities necessary for generation of two *directly interacting* collimated electron beams can not yet be achieved, electron–electron interactions in the ballistic regime can be studied as function of electron temperature using the collimation experiment of Ref.[7]. The sample temperature dependent zero-field collimation signal is in reasonable agreement with an exponential decay $\exp(-L/v_F\tau)$, with $\tau = \tau_{e-e}$ the temperature dependent quasiparticle lifetime calculated from Fermi liquid theory. The experiment, however, shows a somewhat faster decay with temperature than predicted by the Fermi liquid theory, possibly caused by additional temperature dependent *elastic* electron–phonon scattering. Incorporating an elastic electron–phonon scattering rate of 1×10^{10} $s^{-1}K^{-1}$ in $\exp(-L/v_F\tau)$ by $\tau^{-1} = \tau_{e-e}^{-1} + \tau_{e-p}^{-1}$ yields excellent agreement with the experiment. Electron–phonon scattering rates, however, are not accurately known, and experimental derived values, like 3×10^8 $s^{-1}K^{-1}$ as measured by Leadly *et al.*[10], result from *inelastic* scattering. Further studies must reveal whether indeed the complete discrepancy between our temperature dependent collimation signal and Fermi liquid theory can be lifted by incorporation of elastic electron–phonon scattering with a rate of 1×10^{10} $s^{-1}K^{-1}$, or whether the

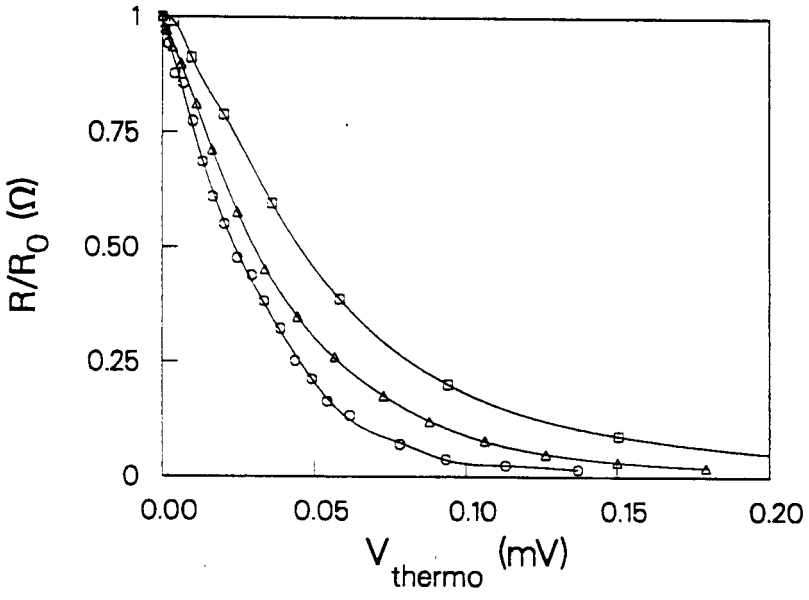

Figure 7.9: Normalized collimation peak signals *vs.* thermovoltage $V_{\text{thermo}} = V_1 - V_6$ for a dc current through the channel (circles) and for a dc current through point contact m, that is set at $N = 4$ (triangles) or $N = 1$ (squares). The solid lines are guides to the eye. The difference between the curves is explained by a deviation from a thermalized Fermi-Dirac electron distribution in the region between i and c, that increases for the subsequent cases. (Sample G620D54).

discrepancy must partly be contributed to a change in point contact conductance with increasing sample temperature.

Nevertheless, the Fermi liquid theory provides a useful description in the new field of electron–electron interactions in the ballistic regime. This was recently also demonstrated by Yacoby *et al.*[25], who studied quantum interference as function of electron excess energy at low temperatures. Assuming that phase is lost by individual electron–electron collisions, they were able to describe the observed decrease in interference signal with increasing excess energy with a phase breaking time equal to the quasiparticle lifetime given by Eq.(7.5).

The collimation signal as function of a current heating the 2DEG has not yet been compared quantitatively with Fermi liquid theory, because the exact value of the electron temperature can not yet be derived from the experimental thermopower of a point contact. Using a more realistic transmission function [32] than the idealized step function for point contacts could possibly meet this deficit, and further studies on this point are underway.

Acknowledgement

I have performed the work presented in this report at the Philips Research Laboratories in Eindhoven, in the group Advanced Theoretical and Experimental Physics, with great pleasure. The last ten months have been a valuable experience for me, because of the opportunity to work in both an exciting field of physics and in an industrial environment. Also the pleasant collaboration with the people in WP made this period unforgettable to me.

In particular, I want to thank Laurens Molenkamp for his sound and stimulating guidance and encouraging support, and for many valuable advices, Menno Mabesoone for teaching me how to deal with low temperatures and non-destructive electrical signals as well as for continuous technical assistance, and Toine Staring for help with all kinds of problems, varying from basal physics to sophisticated LaTeX typography. Furthermore I want to thank Bruce Alphenaar, John Williamson and Rob Eppenga for their help and encouraging cooperation, Eugène Timmering and Hans Buyk for sample preparation and Henk van Houten and Carlo Beenakker for fruitful discussions and useful suggestions. I owe thanks to Ad Nagelkerke and Fred de Wit for constant supply of liquid helium. In addition, I acknowledge Martin Schuurmans and Prof. Dr. A.R. Miedema for allowing me to work at the Philips Research Laboratories in Eindhoven.

Last but not least, I want to thank Prof. Dr. J.H. Wolter for giving me the opportunity to achieve this valuable experience and for stimulating interest in my work.

Bibliography

[1] B.J. van Wees, H. van Houten, C.W.J. Beenakker, J.G. Williamson, L.P. Kouwenhoven, D. van der Marel, and C.T. Foxon, Phys. Rev. Lett. **60**, 848 (1988).

[2] D.A. Wharam, T.J. Thornton, R. Newbury, M. Pepper, H. Ahmed, J.E.F. Frost, D.G. Hasko, D.C. Peacock, D.A. Ritchie, and G.A.C. Jones, J. Phys. C **21**, L209 (1988).

[3] C.W.J. Beenakker and H. van Houten, in: *Solid State Physics*, ed. by H. Ehrenreich and D. Turnbull (Academic Press, New York, to be published).

[4] H. van Houten, C.W.J. Beenakker, and B.J. van Wees, in: *Nanostructure Devices*, a volume of Semiconductors and Semimetals, ed. by M. Reed (Academic Press, New York, to be published).

[5] L.W. Molenkamp, H. van Houten, C.W.J. Beenakker, R. Eppenga, and C.T. Foxon, Phys. Rev. Lett. **65**, 1052 (1990).

[6] M. Büttiker, Phys. Rev. Lett. **57**, 1761 (1986).

[7] L.W. Molenkamp, A.A.M. Staring, C.W.J. Beenakker, R. Eppenga, C.E. Timmering, J.G. Williamson, C.J.P.M. Harmans, and C.T. Foxon, Phys. Rev. B **41**, 1274 (1990).

[8] P.N. Butcher, J. Phys. Condens. Matter **2**, 4869 (1990).

[9] P. Streda, J. Phys. Condens. Matter **1**, 1025 (1989).

[10] D.R. Leadly, R.J. Nicholas, J.J. Harris, and C.T. Foxon, Solid State Electron. **32**, 1473 (1989).

[11] J.J. Harris, J.A. Pals, and R. Woltjer, Rep. Prog. Phys. **52**, 1217 (1989).

[12] L.I. Glazmann and I.A. Larkin, Semicond. Sci. Technol. **6**, 32 (1991).

[13] J.G. Williamson, C.E. Timmering, C.J.P.M. Harmans, J.J. Harris, and C.T. Foxon, Phys. Rev. B **42**, 7675 (1990).

[14] M. Büttiker, Phys. Rev. B **38**, 9375 (1988).

[15] B.J. van Wees, E.M.M. Willems, C.J.P.M. Harmans, C.W.J. Beenakker, H. van Houten, J.G. Williamson, C.T. Foxon, and J.J. Harris, Phys. Rev. Lett. **62**, 1181 (1989).

[16] S. Komiyama, H. Hirai, S. Sasa, and S. Hiyamizu, Phys. Rev. B **40**, 12566 (1989).

[17] B.W. Alphenaar, P.L. McEuen, R.G. Wheeler, and R.N. Sacks, Phys. Rev. Lett. **64**, 677 (1990).

[18] B.J. van Wees, E.M.M. Willems, L.P. Kouwenhoven, C.J.P.M. Harmans, J.G. Williamson, C.T. Foxon, and J.J. Harris, Phys. Rev. B **39**, 8066 (1989).

[19] J.R. Kirtley, Z. Schlesinger, T.N. Theis, F.P. Milliken, S.L. Wright, and L.F. Palmateer, Phys. Rev. B **34**, 5414 (1986).

[20] P.G.N. de Vegvar, A.M. Chang, G. Timp, P.M. Mankiewich, J.E. Cunningham, R. Behringer, and R.E. Howard, Phys. Rev. B **36**, 9366 (1987).

[21] P.C. van Son, G.H. Kruithof, and T.M. Klapwijk, Phys. Rev. B **42**, 11267 (1990).

[22] L.W. Molenkamp, M.J.P. Brugmans, H. van Houten, C.W.J. Beenakker, and C.T. Foxon, accepted for publication in Phys. Rev. B. (Rap. Comm.), May 15 1991 issue.

[23] P.L. McEuen, A. Szafer, C.A. Richter, B.W. Alphenaar, J.K. Jain, A.D. Stone, and R.G. Wheeler, Phys. Rev. Lett. **64**, 2062 (1990).

[24] S. Komiyama, H. Hirai, M. Ohsawa, H. Matsuda, S. Sasa, and T. Fujii, in *Proc. 20th Int. Conf. on the Physics of Semiconductors,* ed. by E.M. Anastassakis and J.D. Joannopoulos (Singapore, 1990), p.1150.

[25] A. Yacoby, U. Sivan, C.P. Umbach, and J.M. Hong, preprint.

[26] J. Spector, H.L. Stormer, and K.W. Baldwin, preprint.

[27] M. Kaveh and N. Wiser, Adv. Phys. **33**, 257 (1984).

[28] D. Pines and P. Nozières, *The Theory of Quantum Liquids* (Benjamin, New York, 1966).

[29] R. Jalabert and S. Das Sarma, Phys. Rev. B **39**, 5542 (1989).

[30] G.F. Giuliani and J.J. Quinn, Phys. Rev. B **26**, 4421 (1982).

[31] L.W. Molenkamp, unpublished results.

[32] M. Büttiker, Phys. Rev. B **41**, 7906 (1990).